Selection of Stainless-Steel Grades for Food Processing based on Pitting Corrosion

Carlos Krawzoff Ramírez

Master Thesis, Production and Materials Engineering,
MMTM05 30 hp, 29th May 2026

LTH
FACULTY OF
ENGINEERING

Industrial and Academic Supervisor: Martin Adell, Technology Specialist, PSE Portfolio Management at Tetra Pak Processing Systems AB
Examiner: Filip Lenrick, Senior Lecturer, Production and Materials Engineering
Author: Carlos Krawzoff Ramírez
Lund, Sweden, 2026

Department of Mechanical Engineering Sciences
Division of Production and Materials Engineering
LTH, Faculty of Engineering
Lund University
Box 118
SE-221 00 Lund,
Sweden

Printed in Sweden
Media-Tryck
Lund University

Abstract

Selecting the right stainless-steel (SS) grade for food processing equipment is a critical decision, since processing environments vary widely and a grade that performs well under one set of conditions may be inadequate under another. The following study evaluates the pitting corrosion resistance of three grades commonly used in the food industry, 316L, 2205 DSS and 254 SMO, under varying chloride concentration, temperature and acetic acid content, with the aim of developing a grade selection matrix for Tetra Pak when introducing new food solution products. The results confirmed a clear pitting resistance hierarchy (254 SMO > 2205 DSS > 316L), with temperature as the most damaging factor, revealing that at 90°C the passive oxide layer of 316L is thermally saturated to the point where further changes in chloride or acid content have negligible additional effect. The most unexpected finding was that acetic acid consistently increased pitting potential in 254 SMO while slightly reducing it in the other two grades, suggesting an inhibitory interaction with this alloy that strengthens its advantage under aggressive conditions. Phenomena such as transpassive dissolution was frequently observed in 2205 DSS and 254 SMO under less aggressive conditions, and crevice corrosion was clearly present in 316L but ambiguous and far less pronounced in the higher-alloy grades. The pitting engineering diagrams developed from these results show promise as a practical selection tool for new food products at Tetra Pak. As a pilot study, the adaptation of welded 254 SMO samples to the experimental setup produced meaningful results that establish a basis for their future integration into the selection matrix.

Preface

This master's thesis was carried out as a collaboration between the Division of Production and Materials Engineering at Lund University and Tetra Pak Processing Systems AB, as part of the final project within the Master's Programme in Production and Materials Engineering, written during the spring semester of 2026. The aim of this work is to contribute to the development of a selection matrix for different stainless-steel grades (316L, 2205 Duplex, and 254 SMO) for food processing equipment based on pitting corrosion behaviour, as well as an exploratory study of welded grades for their future integration into the matrix.

I would like to give special thanks to my supervisor, Martin Adell from Tetra Pak, for guiding me throughout this project and for his valuable advice and discussions, as well as continuous guidance that was essential in moving this work forward. I would also like to thank Magnus Gullberg, Matthias Widen, Janna Mathisson, and Pär Strom from the Heat Exchangers Department at Tetra Pak, for helping me connect this academic work to industry and linking it to real-world needs.

Finally, I would like to thank the workers at the Division of Production and Materials Engineering for their support, and particularly Mikael Hörndahl, for keeping this project running through frequent maintenance and assistance whenever issues arose with the experimental setup.

List of abbreviations and symbols

Abbreviation	Meaning
SS	Stainless Steel
CPDP	Cyclic Potentiodynamic Polarization
XPS	X-ray Photoelectron Spectroscopy
PREN	Pitting Resistance Equivalent Number
HAZ	Heat Affected Zone
BM	Base Metal
WM	Weld Metal
OCP	Open Circuit Potential
E_{corr}	Corrosion Potential
E_{pit}	Pitting Potential
E_{prot}	Protection Potential
E_{v}	Upper Vertex Potential
E_{break}	Breakdown Potential
E_{safe}	Lower Safety Limit
$E_{service}$	Service Potential
E_{α}	Safety factor including operational variability
SHE	Standard Hydrogen Electrode
R_{a}	Surface Roughness
CCT	Critical Crevice Temperature
CPT	Critical Pitting Temperature
SEM	Scanning Electron Microscopy
β	Upper Limit
CIP	Cleaning In Place
SIP	Sterilization In Place
CALPHAD	CALculation of PHAse Diagrams
DFT	Density Functional Theory
EBSD	Electron Backscatter Diffraction
ATR-FTIR	Attenuated Total Reflectance-Fourier Transform Infrared Spectroscopy

List of Figures

List of Tables

Contents

1. Introduction

Material selection has become an increasingly complex and critical process in engineering design, directly influencing manufacturing methods, equipment performance, and long-term operational costs. In food processing industries, stainless steels (SSs) are the most widely used structural materials due to their exceptional combination of mechanical strength, formability, and corrosion resistance [1]. Their versatility allows them to be fabricated into various geometries that satisfy both structural and hygienic standards. Of particular importance is the behavior of metal surfaces in direct contact with food and processing solutions, which must meet strict hygiene and food safety standards [2]. Regular cleaning and maintenance of these surfaces are therefore essential, as neglecting them can lead to material degradation with serious economic and environmental consequences [1, 2].

Among the properties that govern alloy selection for food processing environments, corrosion resistance is of paramount importance. Stainless steels owe their superior resistance to the spontaneous formation of a thin, chromium-rich passive oxide layer on their surface, which acts as a protective barrier against chemical attack. However, this passivity can break down under sufficiently aggressive conditions limiting the applicability of certain SS grades. In food processing environments, high chloride concentrations and elevated temperatures are the primary drivers of such degradation promoting pitting corrosion, a form of localized corrosion that can compromise both equipment integrity and food integrity [1, 3]. Pitting corrosion is particularly damaging because it is difficult to detect and can lead to rapid material failure. Its complexity arises from the interplay of multiple environmental factors, often combinations of several factors, and is further amplified by the inherently stochastic nature of pit initiation. The simultaneous presence of corrosion-promoting and corrosion-inhibiting parameters introduces significant uncertainty, making reliable prediction of pitting behavior a considerable challenge [5].

One well established electromechanical method for assessing pitting and crevice corrosion resistance is the cyclic potentiodynamic polarization (CPP) technique. This method has been previously developed and validated in earlier master´s theses conducted within the same industrial-academic collaboration, where the influence of varying environmental parameters were investigated for the single stainless-steel grade 316L [4, 5].

However, because processing environments vary widely, and can change considerably with the introduction of new food products, an alloy that performs well under one set of conditions may be inadequate under another. This variability underscores the need to systematically compare the corrosion resistance of multiple SS grades across a range of relevant conditions. Selecting the appropriate alloys is essential not only to prevent structural failure but also to enhance food safety and minimize environmental and economic risk associated with equipment degradation [2]. Accordingly, this master´s thesis aims to contribute to the development of material selection guidelines for Tetra Pak by conducting a direct comparative evaluation of 316L, SMO 254 and Duplex 2205 stainless steels under varying food processing conditions, including differences in chloride concentration, temperature, and pH, with the goal of supporting the construction of a practical material selection matrix. Additionally, welded samples were included as an exploratory assessment in this study, to support their adaptation and enable comparison with unwelded samples and thus enhance this matrix.

1.1 Aim of the Thesis

The aim of this master thesis is to compare and evaluate pitting corrosion resistance of three commonly used stainless-steel grades (316L, 254 SMO and 2205 Duplex) under conditions relevant to food processing. It also seeks to adapt and assess a previously developed method [4, 5] by applying it to stainless-steel grades that have not been previously tested. The aim is also to introduce welded 254 SMO samples into this method and study their compatibility with it. The results are intended to contribute to material selection guidelines for Tetra Pak food processing equipment.

1.2 Objectives

The objectives of the following master thesis report can be broken down into:

- Adapt the previously developed method for application to newly introduced stainless steel grades, specifically to 254 SMO and 2205 Duplex.

- Compare and evaluate corrosion resistance of these stainless steels based on different levels of chloride concentration, temperature and Acetic Acid (pH).
- Evaluate in which processing conditions higher-alloyed stainless steels (254 SMO and 2205 Duplex) provide a performance advantage compared to 316L and with each other.
- Investigate the incorporation and adaptation of welded 254 SMO samples withing the method to support future development guidelines for welded SSs.

1.3 Scope and Limitations

This project focuses on a comparative experimental evaluation of three types of stainless-steel grades: austenitic stainless steel 316L, super-austenitic stainless steel (254 SMO), and 2205 Duplex stainless steel. The study is based on experimental electromechanical testing under controlled conditions simulating food processing environment and is subjected to varying different levels of chloride concentration, temperature and pH. The scope of the work is generating comprehensive pitting corrosion performance data that can support the material selection for further decisions and contribute to the development of material selection guidelines for industrial applications at Tetra Pak.

The study is limited to laboratory-scale experiments and a restricted set of Stainless-steel grades and environmental conditions. Only pitting corrosion and crevice corrosion are considered, while other degradation mechanisms relevant to food processing equipment are excluded. The experiments performed in this project are subjected to short-term measurements using a standardized surface sample preparation and therefore it is not considered effects related to manufacturing variability, welding, mechanical loads or long-time exposures. For the exploration of the incorporated welded 254 SMO samples, the surface sample preparation differs from the unwelded samples, in order to be able to study the introduction of welded SSs separately. Furthermore, findings should not be used as a direct but as an indicative and comparative prediction.

1.4 Structure of the Report

The report is divided into the following sections:

Section II): A literature review in three parts: the corrosion phenomena and localized corrosion types relevant to this study, the SS grades investigated, their passive oxide films, alloying elements, and welding considerations, and the electrochemical parameters, absence of corrosion indicators, and experimental setup used throughout this work.

Section III): Experimental strategy of the conditions studied, preparation methods for the samples with and without welding, chemical compositions of the SSs used, as well as the configuration of the setup used for carrying out the corrosion experiments along with the data analysis carried out.

Section IV): Results and discussion of the measured corrosion parameter data, along with their interpretation and curves for each SS grade, followed by an SS grade selection tool. Additionally, an exploratory study of 254 SMO welded samples is presented, including results and discussion of their suitability for the setup used.

Section V): Project conclusions about the findings and possible improvements.

Section VI): Future guidelines for the improvement of the method, suggestions for new trials under the same setup, as well as subsequent studies to confirm different phenomena.

2. Background

In this section, corrosion and its measured types are introduced alongside the SS grades used, including their chemical composition, alloying elements, and effect on corrosion resistance. Welding effects, corrosion parameters, absence of localized corrosion, and the experimental setup are also covered.

2.1 Corrosion in Stainless Steel

Corrosion is a natural process by which metals progressively degrade, reducing their functional lifetime. It occurs through electrochemical reactions between the metal and its surrounding environment, involving species such as

oxygen, water or other chemical components, which modify material properties and ultimately lead to loss of functionality [6].

For corrosion to occur, four conditions must be met simultaneously: an anodic region where oxidation takes place, a metallic bridge through which electrons are transported, a cathodic region where reduction occurs, and an electrolyte enabling ion transport [6]. When all four are present, an electrochemical corrosion cell is established. Depending on the environment, corrosion products may include iron ions, iron hydroxides, oxyhydroxides, oxides or carbonates [6].

Thermodynamics governs the spontaneity of these reactions through the Gibbs free energy (ΔG): when ΔG is negative, corrosion proceeds naturally; when positive, external energy input is required [7]. Beyond thermodynamics, kinetics determines the rate of metal dissolution and therefore the material lifespan, a rate that can be significantly accelerated by factors such as high pressure and, to a lesser extent, temperature [7, 8]. Environmental variables including chloride concentration, temperature and pH further influence both the speed and the type of corrosion mechanism that develops at the metal surface [7].

When a metal is immersed in an electrolyte, anodic and cathodic regions form naturally (Figure 1), generating local electrochemical cells in which electrons flow through the metal while ions migrate through the electrolyte [9].

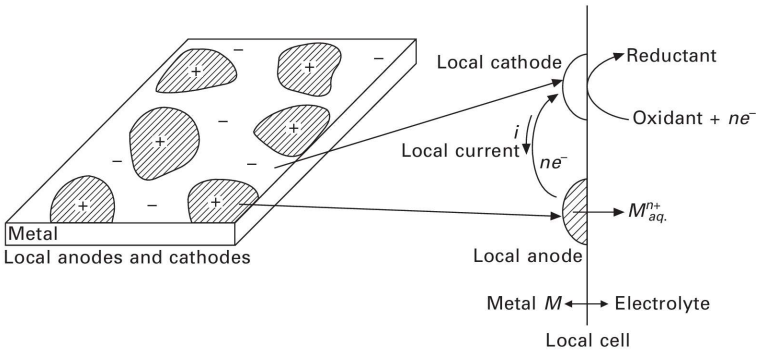

Figure 1: *Schematic illustration of general corrosion, where some regions behave as anodes and others as cathodes, creating local zones depending on the metal and the solution. At a local anode, the metal dissolves (oxidation) and releases electrons that travel to the local cathode, where, depending on the solution, the electrons react in the reduction process [9].*

The anodic region undergoes metal dissolution, expressed for iron as:

$$Fe \rightarrow Fe^{2+} + 2e^{-} \quad (1)$$

At the cathodic region, electrons are consumed through reduction reactions that vary with solution pH. In acidic environments, hydrogen ion reduction occurs:

$$2H^{+} + 2e^{-} \rightarrow H_2 \quad (2)$$

In neutral or alkaline environments, dissolved oxygen is reduced:

$$O_2 + 2H_2O + 4e^{-} \rightarrow 4OH^{-} \quad (3)$$

These reactions balance each other, reaching a steady state known as the corrosion potential, at which corrosion proceeds at a rate determined by the corrosion current [9].

Corrosion manifests in two broad forms. In general or uniform corrosion, the anodic and cathodic regions continuously shift across the entire metal surface, producing relatively even material loss over time, with no clear distinction between anodic and cathodic regions [10]. In contrast, localized corrosion concentrates the electrochemical attack at random positions, with small anodic areas developing while the remainder of the surface acts as cathode, leading to mechanisms such as pitting or crevice corrosion [7]. The following sections focus on these two forms of localized corrosion, which are the most relevant to this work.

2.1.1 Localized corrosion

Localized corrosion occurs at random positions on the metal surface, driven by surface heterogeneities such as grain boundaries or inclusions, or by aggressive species in the surrounding environment [11, 12]. Unlike uniform corrosion, the fixed nature of the attack concentrates stress at a single point, which can lead to cracking under an applied force. The difficulty in predicting when and where it initiates makes it particularly challenging and complex to prevent [11, 12].

2.1.1.1 Pitting corrosion

Pitting corrosion is a form of localized corrosion that initiates on an open metal surface, leading to rapid formation of small holes or pits while the surrounding surface remains unattacked [6, 10]. It is considered one of the primary causes of component failure and deterioration, particularly in the food and pharmaceutical industries, where aluminium alloys, nickel-base alloys, titanium and stainless steels are widely used. In these applications, even a small localized loss of material can lead to irreparable damage [10]. Passive materials are especially susceptible due to the nature of their protective oxide layer.

Pitting is particularly prevalent in environments containing aggressive ions such as Br^-, I^-, thiosulfate or Cl^-, the latter being the focus of this work [10]. For example, chloride ions are highly mobile and tend to accumulate at weak points on the passive film, such as surface irregularities or defects, progressively weakening the protective layer until localized penetration occurs. The result is a surface that is electrochemically active within the pit while remaining passive elsewhere [10]. Since pit propagation occurs in subsurface, it often proceeds without any visible external indication, making pitting particularly critical [10].

Passive film breakdown can occur through several proposed mechanisms, including penetration, adsorption and film rupture mechanisms. Regardless of the mechanism, the result is exposure of the underlying metal to the electrolyte, enabling anodic dissolution within the pit (Figure 2). The process develops across three sequential stages:

Stage 1: Initiation through passive film breakdown. Local breakdown of the passive oxide layer exposes the underlying metal. In the case of iron, hydrated oxides react with chloride ions through a cyclic process that regenerates Cl^- and progressively lowers the energy barrier for pit nucleation:

$$FeOOH + Cl^- \rightarrow FeOCl + OH^- \quad (4)$$

$$FeOCl + H_2O \rightarrow Fe^{3+} + Cl^- + 2OH^- \quad (5)$$

Stage 2: Metastable pit growth and repassivation. Following initiation, small metastable pits nucleate and grow until local conditions are insufficient to sustain them, at which point repassivation occurs. These events appear in electrochemical measurements as brief current spikes during polarization methods. Metastable pits serve as precursors to stable pit formation and indicate preferential sites for further attack.

Stage 3: Stable pit growth and propagation. When local electrochemical conditions inside the pit become sufficiently aggressive through high chloride concentration or acidic accumulation, the pit transitions to stable autocatalytic growth. Metal cation accumulation drives hydrolysis:

$$Fe^{2+} + 2H_2O \rightarrow Fe(OH)_2 + 2H^+ \quad (6)$$

The resulting decrease in local pH is sustained by continuous chloride ingress to maintain charge neutrality. Simultaneously, oxygen reduction proceeds on the external cathodic surface:

$$O_2 + 2H_2O + 4e^- \rightarrow 4OH^- \quad (3)$$

Together, these reactions maintain the electrochemical cell driving pit propagation into the bulk material [10, 13].

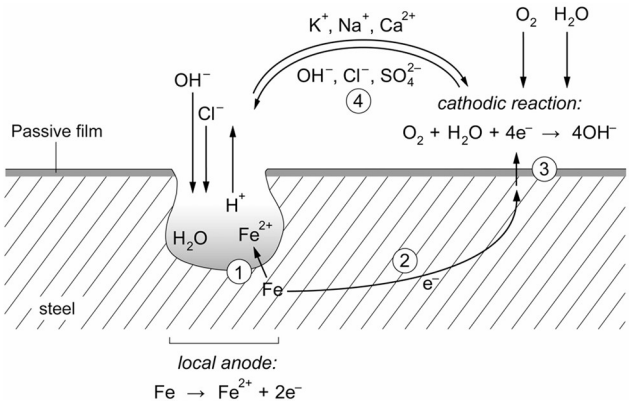

Figure 2: *Schematic illustration of pitting corrosion. (1) The protective layer is destroyed at the local anode by pitting, and the metal begins to dissolve, releasing electrons that travel through the metal (2) to the local cathode (3), where they are consumed to produce OH- ions. The ions in solution (4) move to balance the electrical charges between both local regions, closing the electrochemical circuit [14].*

2.1.1.2 Crevice Corrosion

Crevice corrosion is a form of localized corrosion that initiates within confined geometrical spaces such as cavities, gaps, grooves or cracks, particularly in areas where two surfaces are in contact [15]. These spaces allow solution to enter but restrict its circulation, reducing the available oxygen and promoting ion accumulation, creating a local environment more aggressive than the surrounding bulk solution. Because the attack progresses in hidden areas, it can cause equipment failure without prior visible indication [15].

Stage 1: Initiation through oxygen depletion. Upon immersion, anodic and cathodic reactions initially occur uniformly across the metal surface:

$$Fe \rightarrow Fe^{2+} + 2e^{-} \quad (1)$$

$$O_2 + 2H_2O + 4e^{-} \rightarrow 4OH^{-} \quad (3)$$

As exposure continues, oxygen within the crevice is consumed by diffusion-limited cathodic reduction and cannot be replenished. Once depleted, cathodic reactions cease inside the crevice, establishing a differential aeration cell in which the crevice interior becomes the anodic region and the external surface acts as cathode.

Stage 2: Propagation through chloride accumulation and acidification. Anodic dissolution produces Fe^{2+} ions that accumulate and undergo hydrolysis:

$$Fe^{2+} + 2H_2O \rightarrow Fe(OH)_2 + 2H^{+} \quad (7)$$

The increase in H^{+} lowers the local pH and destabilizes the passive film, preventing repassivation. Chloride ions then migrate into the crevice to maintain electroneutrality:

$$Fe^{2+} + 2Cl^{-} \rightarrow FeCl_2 \quad (8)$$

The combined effect of oxygen depletion, metal ion accumulation, local acidification and chloride enrichment creates an autocatalytic environment that accelerates metal dissolution and sustains the attack.

Stage 3: Reduction of crevice aggressiveness. Under certain conditions the process may decelerate if oxygen is reintroduced, ion and acid concentrations decrease, or the geometry permits renewed solution exchange, allowing repassivation of the metal surface and eventually halting the attack [10, 15].

2.2 Stainless Steel Grades

Stainless steels (SSs) are Fe-based alloys widely used across industries due to their good mechanical properties, high hardness, reasonable machinability and the wide variety of geometries in which they can be manufactured [1, 2]. Their corrosion resistance originates from a minimum chromium content of 13 wt% [16], which enables the formation of a self-protecting nanometric oxide layer of at least 2 nm thickness on the metal surface [10]. The higher the Cr content, the greater the corrosion resistance conferred by this passive film.

The passive layer has been characterized through XPS analysis and is commonly described as a bilayer structure [16]: an inner Cr-enriched layer (p-type semiconductor), present as Cr_2O_3 or $Cr(OH)_3$, which provides the primary protective function, and an outer iron oxide layer (n-type semiconductor), found as Fe_2O_3 or FeOOH. The semiconducting behaviour of this bilayer, whether p-type, n-type or mixed p-n, varies with the applied potential [16, 17]. The p-type character of the Cr-rich inner layer is particularly relevant: holes act as charge carriers, trapping electrons and reducing electronic conductivity, which in turn enhances corrosion resistance [17]. In contrast, the n-type outer layer increases electronic conduction and offers comparatively lower protection [17]. Two theoretical frameworks have been proposed to describe passivity in SSs: the Oxide Film theory, in which a protective oxide forms on the metal surface [18], and the Adsorption theory, in which passivity arises from the adsorption of organic anions onto the surface, limiting metal dissolution without necessarily requiring oxide formation [19]. The formation and stability of the passive layer can be further described through the Point Defect Model and the Bipolar Model [16, 17].

Beyond chromium, other alloying elements contribute significantly to corrosion resistance. Molybdenum acts as an inhibitor against localized corrosion, but only when sufficient Cr is present in the alloy [20]. Two mechanisms have been proposed for its role: Mo may stabilize and modify the passive layer directly, or it may reduce the active dissolution rate and limit corrosion propagation [20]. Nitrogen, nickel and copper also improve corrosion resistance [20]. A comparative index widely used to rank pitting resistance among SS grades is the Pitting Resistance Equivalent Number (PREN) [21]:

$$PREN = \%Cr + 3.3 \times (\%Mo + 0.5 \times \%W) + 16 \times \%N \quad (9)$$

This index provides an orientative ranking but does not account for factors such as surface roughness, inclusions, defects or local variations in the passive layer, all of which play a role in practical pitting initiation [22]. The cost of SSs increases with alloying element content, particularly Cr, Mo and Ni, making the selection of a grade a balance between corrosion performance, machinability and cost [23]. The three grades investigated in this work, 316L, DSS 2205 and 254 SMO, represent three distinct levels of alloy complexity, corrosion resistance and cost, and are introduced individually below.

2.2.1 316L (EN 1.4404)

316L is an austenitic stainless steel with a single-phase face-centred cubic (FCC) microstructure [24]. It contains 17–19% Cr and up to 2% Mo, and is distinguished from standard 316 by its reduced carbon content (C < 0.03% vs. C < 0.08%), which limits the formation of chromium carbides ($Cr_{23}C_6$) at grain boundaries and improves resistance to sensitisation and intergranular corrosion [24]. The combination of austenitic structure and Mo content provides good toughness, solid resistance to localized corrosion in chloride environments, and good weldability [25]. The alloy can be cold-worked to increase strength. Compared to 304 SS, 316L offers superior performance in corrosive environments due to its higher Mo content [26], although DSS 2205 has been shown to outperform 316L in marine environments, where a lower density of inclusions in 2205 limits pitting initiation sites [27]. In corrosive media, pitting in 316L tends to initiate preferentially at MnS inclusion dissolution sites [28]. Among the three grades studied here, 316L represents the most cost-effective option with adequate corrosion resistance for moderately aggressive conditions [23].

2.2.2 2205 Duplex (EN 1.4462)

DSS 2205 is the most widely used duplex stainless steel and is characterized by a dual-phase microstructure of approximately equal proportions of austenite and ferrite, which together maximize both mechanical performance and corrosion resistance [21]. A typical example of this dual phase is shown in Figure 3. This phase balance is achieved through controlled heat treatment and quenching: the ferrite phase is stabilized by Cr and Mo, while austenite is stabilized by Ni and N [29]. The alloy contains approximately 22% Cr, up to 3% Mo, around 5% Ni and elevated nitrogen, giving it a yield strength approximately twice that of austenitic SSs [21, 30], though with lower toughness [31].

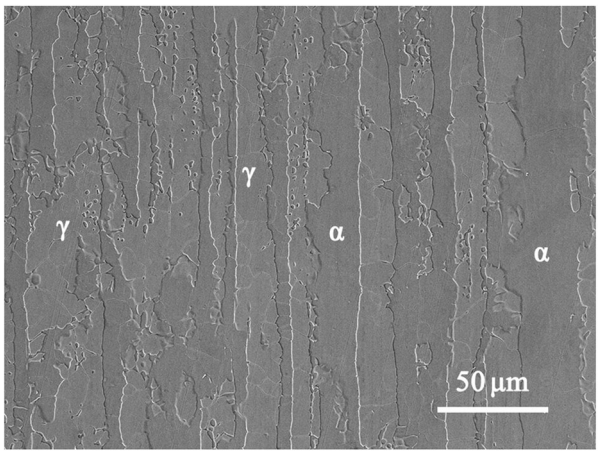

Figure 3: *Typical microstructure obtained of 2205 Duplex showing dual-phase distribution of both austenite (γ) and ferrite (α) in approximate similar proportions of each phase [32].*

The Mo content of up to 3% extends the passive potential range and helps prevent crevice corrosion, although excessive Mo at elevated temperatures can promote the formation of undesirable intermetallic phases such as χ and σ [30]. Nickel acts as an austenite stabilizer; excessively high Ni levels shift the phase balance towards austenite, concentrating Cr and Mo in the remaining ferrite and potentially promoting α' phase formation, which embrittles the material [33].

The two phases do not exhibit equal resistance to localized corrosion. PREN calculations show that ferrite, enriched in Cr and Mo, achieves a higher PREN than austenite, which is richer in Ni and N [31]. However, nitrogen solubility is approximately six times lower in ferrite than in austenite, and excess nitrogen leads to nitride precipitation at grain boundaries, locally reducing corrosion resistance [31]. Under inadequate casting or heat treatment conditions, Cr and Mo segregate to the ferrite grain interiors, leaving grain boundaries and ferrite–austenite (α/γ) and ferrite–sigma (α/σ) interfaces as preferential pitting initiation sites [31]. Studies conducted under hydrogen-containing environments have reported the opposite behaviour, with austenite showing higher passive layer conductivity than ferrite and grain boundaries exhibiting the highest conductivity of all, making them the most susceptible sites [34]. This apparent contradiction across studies reflects the sensitivity of localized corrosion initiation to specific environmental conditions. Regardless of the phase attribution, grain boundaries are consistently identified as weak points for pitting initiation [22, 34]. One study on two variants of DSS 2205 found that pitting initiation was dominated not by either phase but by complex Ca-rich oxide inclusions, highlighting the limitations of PREN as a sole predictor of pitting resistance [22]. It is also significant noting that the poor grindability of DSS 2205 compared to 316L, reflected in higher average surface roughness, porosity and surface defects after preparation [35], introduces additional variability in corrosion testing and must be considered when interpreting electrochemical results.

2.2.3 254 SMO (EN 1.4547)

254 SMO is a super austenitic stainless steel (SASS) with a single-phase FCC austenitic microstructure. Its exceptional corrosion resistance is attributed to its high molybdenum content of approximately 6%, combined with elevated levels of Cr, Ni and N compared to conventional 300-series grades [36]. These alloying additions provide a significant improvement in resistance to localized corrosion, making 254 SMO suitable for aggressive environments where standard grades such as 316L would be insufficient [37, 38]. Its corrosion resistance approaches that of nickel-base alloys [38]. A key limitation of this grade at elevated temperatures is an increased tendency to form intermetallic precipitates, including σ, χ and Laves phases, which can locally degrade corrosion resistance [38]. Among the three grades evaluated in this work, 254 SMO represents the highest alloy content, greatest corrosion resistance and highest cost.

2.2.4 Welding of austenitic stainless steels

Welding austenitic stainless steels such as 254 SMO is naturally challenging. When welding, three common zones can be distinguished, which are the weld metal (WM) which melts and forms the weld bead, the heated affected zone (HAZ) which its microstructure is affected due to the heat of the welding and the base metal (BM), which is the region that is not affected by the heat of the welding. The low thermal conductivity of austenitic

alloys limits heat dissipation during the welding process and affects solidification behaviour, while the high thermal expansion coefficient increases the risk of distortion and residual stress [39, 40]. These characteristics make microstructural changes and defect formation, particularly in the welding metal zone (WM) and the heat-affected zone (HAZ), difficult to avoid.

In pulsed current gas tungsten arc welding (PC-GTAW), heat input (HI) is one of the most critical process parameters. High HI values tend to increase the number of microstructural defects, while lower values are generally more beneficial, reducing the extent of the HAZ and improving weld quality overall [40]. Compared to conventional GTAW (known as TIG), PC-GTAW also reduces elemental segregation due to the pulsed current and associated cooling periods, though some depletion of elements such as Mo and Cr at the weld line can still occur during cooling, making the weld region more susceptible to localized corrosion from an electrochemical point of view [40]. Studies using PC-GTAW on 254 SMO have reported no formation of sigma, mu or Laves phases [40], which is an important advantage for maintaining corrosion resistance. The pulsed current approach also promotes a finer microstructure compared to continuous current methods [41], though Mo segregation at grain boundaries in the weld metal has been observed in stainless steels such as 254 SMO [41].

In TIG welding a shielding gas, which is typically argon or helium, is directed from the torch body onto the molten metal to prevent contact with atmospheric oxygen and nitrogen, both of which can damage the microstructure of the weld. Argon is generally preferred due to its higher density and better resistance to atmospheric disturbances [39]. When the weld is performed without a shielding gas, a phenomenon known as heat tint develops on and around the weld surface, caused by the formation of surface oxides [42]. The colour of the heat tint varies with temperature and degree of oxidation, where lighter colours can indicate less thermal damage, while darker regions, such as dark blue or black, correspond to heavier oxidation [43]. From a corrosion perspective, welding without shielding gas leads to the growth of a Cr-rich oxide layer at the surface, which depletes chromium in the surrounding metal. This leaves subsurface zones with reduced Cr content that are more susceptible to localized corrosion [43]. The oxide layer itself on the weld metal is porous and discontinuous, providing preferential sites for chloride ion attack [44].

The question of whether to grind the welded surface before electrochemical testing is not trivial. Grinding removes the surface oxides and heat tint, which tends to improve the measured pitting resistance [42, 44], and studies using CPDP on welded samples have generally found more reliable polarization curves after grinding [45]. However, grinding also introduces surface deformation that can reduce passive film thickness and potentially worsen corrosion resistance [46]. When no shielding gas is used and heat tint is present, the balance tends to favour grinding, since the oxide layer significantly modifies the electrochemical response and difficulties the determination of when corrosion happens [42]. Studies such as [42], where no backing gas is used, resolve this by grinding both the HAZ and WM separately with 600 SiC paper after welding, including flattening the welding line to the surrounding surface level before testing.

2.3 Electrochemical parameters

2.3.1 Electrochemical Testing Methods

Electrochemical techniques are widely used to assess corrosion resistance of metals by measuring reactions at the metal-electrolyte interface. These techniques provide a rapid, up to a few minutes, and sensitive information about corrosion kinetics, passive film formation and breakdown, and electrolyte changes [47]. Compared to conventional approaches such as weight-loss measurements, which may take several days to yield results, electromechanical techniques enable significantly faster assessment and real-time monitoring of corrosion processes [47, 48].

Measurements are conducted using a three-electrode electromechanical cell, in which potential is carefully applied to the metal and controlled while the resultant current is simultaneously recorded. The cell compromises three components: a working/sample electrode (WE), typically the metal or alloys sample under investigation, a reference electrode (RE), which provides a stable potential against which the WE potential is measured and a counter electrode (CE) to measure the current at the corresponding applied potential, that completes the circuit and allows the current flow. Lastly, an electrolyte is used to replicate environmental conditions relevant to the application interest [49].

2.3.2 Open Circuit Potential (OCP)

Prior to any electromechanical measurement, the Open Circuit Potential (OCP) is measured to establish a baseline for the system. The OCP, also referred as the corrosion potential (E_{corr}), represents the steady-state potential at the metal-electrolyte interface when no external current is applied. It can also be described as the "natural" potential at which corrosion occurs on metals. Under this condition, anodic and cathodic reactions proceed at equal rates, reaching an electromechanical equilibrium [50, 51].

Monitoring the OCP over time reveals the evolution of the metal surface, particularly the formation and stabilization of the passive oxide layer, which directly governs corrosion susceptibility [52]. Although this method is fast, measuring this potential is influenced by several variables, including alloy composition, surface preparation, temperature, chloride concentration, and the presence of inhibitors [51, 52]. From a graphical point of view, OCP/E_{corr} corresponds to the intersection between anodic and cathodic polarization branches, with the corrosion current density (I_{corr}) defined at this same point [53]. A practical consideration during measurement is the ohmic drop generated by the electrolyte resistance, which can distort recorded potentials as current flows. This is reduced by placing the reference electrode (RE) as close as possible to the working electrode (WE) [4, 10].

Several factors can alter the measured time of the OCP, such as material properties, electrolyte conditions, and surface preparation. The stabilization time is particularly associated with the formation and steady-state establishment of the passive oxide layer [52]. In studies involving API X65 steel in a 3.5% NaCl solution, OCP evolution was measured for up to 24 hours, before a stable potential was reached, indicating progressive layer stabilization over time [54]. In contrast, studies using platinum electrodes in aqueous solutions suggest that OCP can be determined in as little as 30 minutes, when no significant variation in potential is observed over time [55].

2.3.3 Cyclic potentiodynamic polarization (CPDP)

Cyclic potentiodynamic polarization (CPDP) is an electromechanical technique used to determine the corrosion resistance of metals and alloys, including those capable of repassivation, within a relatively short time [28].

Prior to the measurement, the prepared specimen is immersed in the test solution, and the system is purged for one hour to remove dissolved oxygen. The OCP is then monitored until stabilization is reached, defined as a potential variation of less than 3mV/min. Once a stable OCP is established, the polarization scan begins from this value. A slow scan rate of 1.66 mV/s (±5%), in accordance with ASTM standards, is applied to allow sufficient time for pit nucleation and propagation at each potential [56]. The scan direction is reversed upon meeting one of two criteria: either the threshold current density (i_t=5 mA/cm²) is reached, or the vertex potential (E_v) is attained [56]. The reverse scan then continues until the initial OCP/E_{corr} is reached.

Interpretation of the resulting polarization curve involves several key parameters: the pitting potential (E_{pit}), the repassivation or protection potential (E_{prot}), and the corrosion potential (E_{corr}) [56]. These values are empirical and setup dependent, meaning they may vary under different experimental conditions. When assessing pitting corrosion in alloys, E_{corr} serves as a reference point, but it is E_{pit} and E_{prot} that hold the greatest diagnostic significance, as they directly reflect the material´s resistance to pit initiation and its capacity for repassivation [56]. In practice, the polarization scan typically begins slightly below the measure OCP. Although E_{corr} and OCP are theoretically equivalent, they may diverge in practice.

Once the scan is initiated, the polarization curve can be interpreted through several characteristic regions that reflect the electromechanical state of the metal surface at each applied potential. An example is displayed in Figure 4. The scan begins in in the cathodic region until it reaches E_{corr} (equilibrium between cathodic and anodic reactions), switching then to the active region, where current density rises sharply as the metal surface dissolves and ions pass into the solution [57]. This is usually followed by the active-passive transition, during which the current density decreases as a protective oxide layer progressively forms on the metal surface, gradually suppressing further dissolution [57]. In the following passive region, the current density remains relatively constant, reflecting a significant reduced corrosion rate sustained by the integrity of the passive film [57].

Within this passive region, transient current oscillations may occasionally appear, corresponding to the nucleation and temporary growth of metastable pits at local weaknesses in the passive film. These pits repassivate rapidly due to insufficient acidic chloride accumulation within the pit environment, preventing them from developing into stable corrosion sites [56]. If conditions become sufficiently aggressive, beyond the passive region, a sharp

current increase marks a breakdown of the passive film, which is irreversible, and which points stable pitting corrosion, identified as E_{pit} [56]. Above this potential, the chemistry within active pits is sustained and new pits nucleate and propagate freely [56].

Pit growth continues until the scan is reversed, at which point a hysteresis loop begins to form, providing critical information about the material´s repassivation behavior. The scan finishes either at closing the loop or at returning to E_{corr} [56]. A positive hysteresis occurs when the current density in the reverse scan is higher than in the forward scan, indicating that localized corrosion has taken place and that the metal struggles to repassivate [56]. The reverse scan continues until it crosses the forward curve, and this intersection defines E_{prot}, the lowest current density point reached during the return scan. In contrast, a negative hysteresis, where the reverse scan current remains lower than in the forward scan, indicates that no stable localized corrosion occurred during the measurement [56].

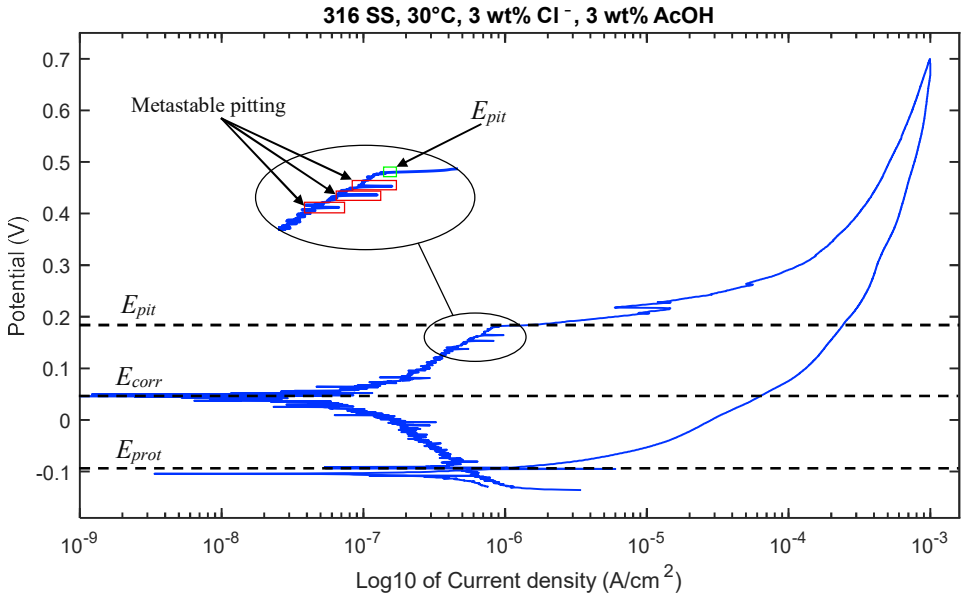

Figure 4: *A typical example of a complete CPDP curve is shown. In the forward scan, the potential increases in the cathodic branch to E_{corr}. As the current increases in the anodic branch, metastable pits form in the passive region, eventually reaching a stable pit formation (E_{pit}). The scan finalizes at E_{prot}, which being lower than E_{corr}, indicates difficulty for repassivation. The hysteresis confirms localized corrosion.*

The relative positions of E_{prot} and E_{corr} therefore provide a practical measure of localized corrosion susceptibility, with the potential difference between E_{pit} and E_{prot} reflecting the overall extend of attack. When E_{prot} is higher than E_{corr}, pit propagation has a higher probability to stop once the scan is reversed, and no new pits form or grow between these two potential values. When E_{prot} is lower than E_{corr}, however, repassivation does not fully occur and existing pits tend to continue growing [56]. Additionally, the behaviour of the current density immediately after scan reversal provides additional insights: if it rises, pits then to actively grow, whereas if it drops, pit growth is slowing down and tends to stop once E_{prot} is reached [56].

2.3.4 Oxygen Evolution and Transpassive Breakdown

Pourbaix diagrams are potential-pH maps used to determine whether a metal is stable, corroding, or protected by an oxide layer (see Figure 5). The metallic "Cr" region is immune to corrosion, while regions such as Cr^{2+}/Cr^{3+} indicate active dissolution. The passive region in these diagrams corresponds to Cr_2O_3, where chromium remains stable over a range of potentials and pH values, with very low dissolution (passive current). As potential increases, chromium enters the transpassive region, where Cr(III) oxidizes to Cr(VI), forming species like CrO_4^{2-} or $HCrO_4^-$ depending on pH, and the passive oxide dissolves into soluble Cr(VI). Potentials in these diagrams are referenced against the Standard Hydrogen Electrode (SHE).

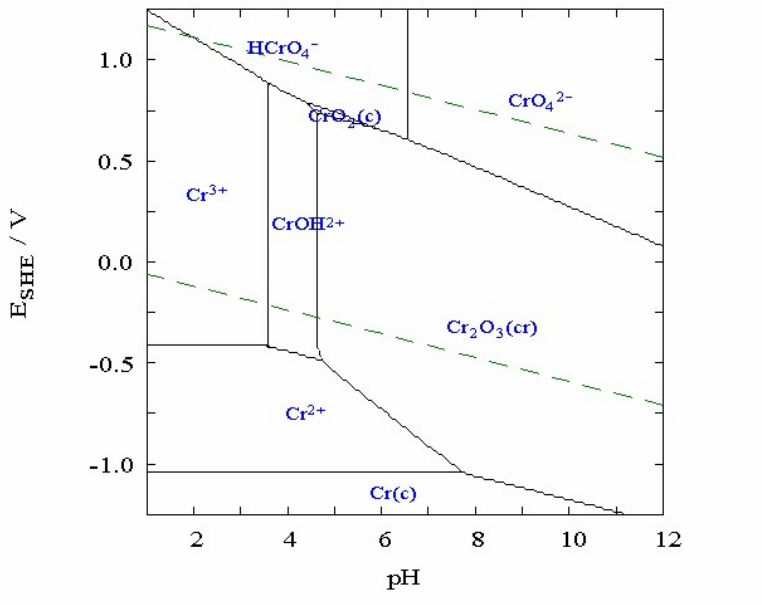

Figure 5: *Pourbaix diagram for Cr in water at 25℃ [58].*

A sudden increase in current density does not always mean pitting corrosion. It can also result from two other phenomena: (1) oxygen evolution, caused by water decomposition ($2H_2O \rightarrow O_2 + 4H^+ + 4e^-$), and (2) transpassive film breakdown, where the passive oxide dissolves. Both are visible in the Pourbaix diagram, where oxygen evolution occurs above the water stability line (upper green dashed line), and transpassive breakdown follows at even higher potentials. Potentials above ~1.0 V vs. SHE requires careful interpretation in this study, as the threshold depends on both potential and pH, among other conditions. This distinction is especially relevant for high-alloy stainless steels (2205 DSS and 254 SMO SS). Due to their strong corrosion resistance, these grades often do not undergo pitting at lower potentials, so a current rise at high potentials is more likely linked to passive film dissolution combined with oxygen evolution, rather than localized corrosion [10, 58].

2.3.5 Test processing unit (Sören)

The CPDP experiments were carried out using an Armfield FT74 pasteurizer, *Sören*. This is a small-scale tubular heat exchanger unit designed to replicate real food processing conditions, capable of heating food solutions up to 150°C and maintaining continuous flow rates across experiments. The unit heats and cools solutions through the tube wall, where the food solution flows inside the tube while the heating or cooling water circulates on the outside. Operating parameters such as temperature and flow rate are controlled through the panel, which also displays readings from temperature and pressure sensors distributed throughout the circuit. A pressure relief valve is as well in the circuit to prevent excessive pressure build up and to avoid product boiling.

The CPDP method on this pasteurizer was first developed and validated for this unit in a previous master's thesis [4], and further confirmed in a subsequent study involving milk processing [5].

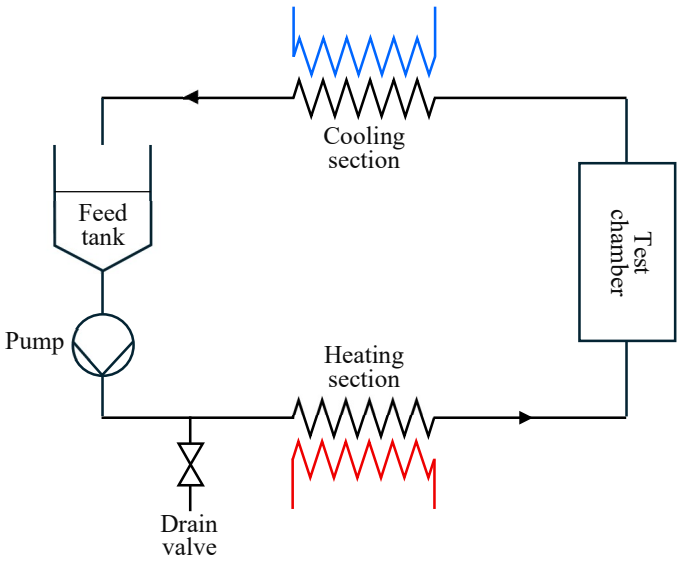

Figure 6: *Schematic illustration of the cycle, where the solution introduced into the feed tank is pumped to the hot section, passes through the test chamber where CPDP tests are performed. The solution is then cooled until it reaches the feed tank where the cycle is repeated. At the end of the experiment, the solution is removed through the drain valve.*

The food solution is loaded into a feed tank (maximum capacity 5 L) and pumped through the heating and cooling sections in a closed loop, returning to the feed tank after each cycle (see Figure 6 and 7). A drain valve after the feed tank and pump, allows removing the solution at the end of each experiment. Between the heating and cooling sections there is a test chamber (Figure 8), developed previously [4], where all electrochemical measurements are performed. SS samples are inserted into the test chamber at the start of each experiment. Additionally, a potentiostat, connected to the test chamber via electrodes and to a computer running a software, was used to conduct the measurements. As mentioned in previous work using this setup, crevice corrosion may occur since no Avesta cell is used since distilled water is not injected at the O-ring contact zone [4].

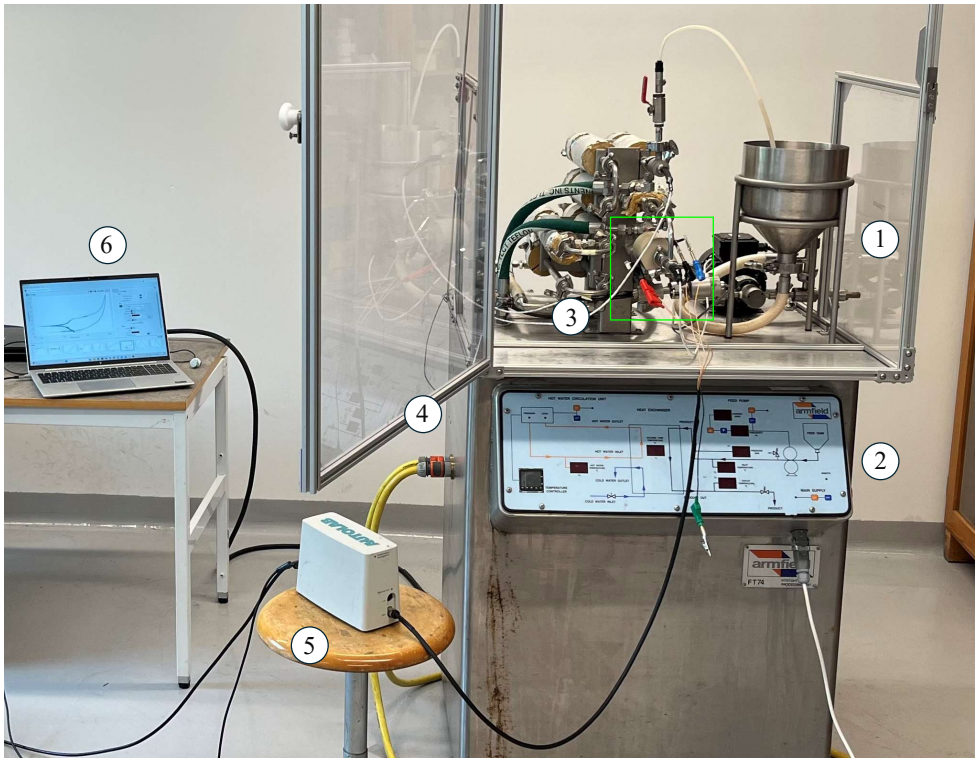

Figure 7: *Test processing unit (Sören) and setup: (1) Pasteurizer. (2) Temperature and flow are controlled in the panel. (3) Test chamber. (4) Supply of cold water. (5) Potentiostat. (6) Software at computer to control and measure CPDP.*

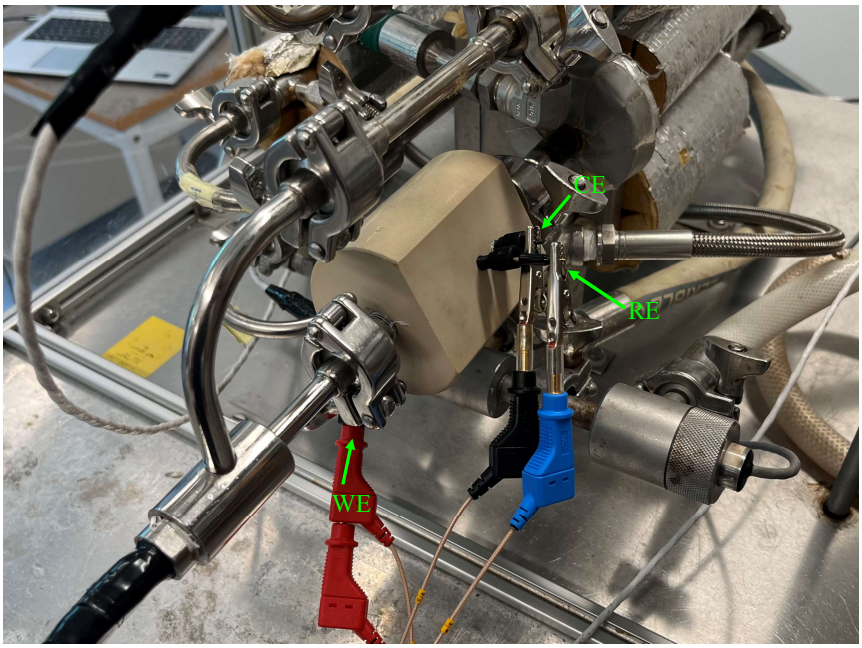

Figure 8: *Test chamber mounted into the pasteurizer and three electrodes attached to it. Solution enters the test chamber after being heated and then is cooled.*

3. Method and Experimental Design

This section covers the experimental conditions, sample preparation for welded and non-welded specimens, chemical composition of the SS grades, and the electrochemical cell setup connected to the pasteurizer and potentiostat. Electrolyte composition and post-experiment analysis tools are also described.

3.1 Experimental Strategy

The experimental design adopted in this project follows a full factorial combination approach, implemented though MATLAB´s *fullfact* function. This methodology was chosen since it allows all possible combinations of the selected factors and their levels to be systematically tested, providing a comprehensive picture of how each variable, and their interactions affect corrosion behavior.

The three stainless steels selected for this study are 316L, 2205 DSS, and 254 SMO. These alloys were chosen since they represent a wide and meaningful performance spectrum withing the food processing industry, where they are commonly found in equipment such as heat exchangers, tanks, and pipping systems. 316L is widely used due to its cost-effectiveness and adequate performance in moderately corrosive environments, while 254 SMO sits at the other end of the spectrum, offering superior corrosion resistance at a considerably high cost.

Three main factors were investigated: chloride concentration, temperature, and acetic acid content (pH). Each factor was defined at two levels (low and high), selected to reflect realistic conditions that food processing units routinely encounter, encompassing many food solutions, which have conditions similar to the experimental ones and values close to those studied. For chloride concentration, 1000 ppm (0.1%) and 30,000 ppm (3%) were chosen to represent low and high salinity environments, respectively. Temperature levels of 30ºC and 90ºC capture the range from mild conditions to elevated thermal loads present in many real-life processing operations. Finally acetic acid (AcOH) content was set at 0% and 3%, being the highest concentration relevant since it lowers the pH of the solution, making it chemically more aggressive toward metallic surfaces. A range of temperature levels and chloride concentration for 316L were explored in earlier projects conducted using the same electromechanical setup [4, 5].

Since corrosion is a stochastic variable and does not always behave the same way twice, each combination was tested three times using electromechanical measurements. This ensures the results are consistent and not due to a single event. The purpose of the following design setup is to study how these three SSs really perform when exposed to conditions that reflect what they would face in actual food processing environments.

For the welded samples study, 254 SMO SS grade was selected, which is often used in welded configurations in the industry. It was tested only under aggressive processing conditions (90°C, 3% Cl^-, no AcOH) to evaluate its suitability within the same setup used for unwelded samples. The goal was to assess whether the results are comparable and to identify potential improvements for future work to enhance reproducibility and enable a meaningful comparison of corrosion parameters between welded and unwelded conditions.

3.2 Sample Preparation

This section shows the method for preparing surface samples with and without welding.

3.2.1 Sample preparation of base metal 316L SS, 2205 DSS and 254 SMO

Samples of 316L, DSS 2205 and 254 SMO were cut from bars into cylindrical specimens of Ø12 × 13 mm. After cutting, the surfaces were manually filed to remove edge irregularities and subsequently ground using Struers Waterproof SiC Foil 220 (68 µm) at 200 rpm with water until a uniformly ground surface was achieved across the entire sample. Grinding was carried out in batches of 10 samples using a sample holder. Samples were then cleaned and dried with distilled water before inspection under an optical microscope.

Surface roughness (R_a) was measured in accordance with ISO 4287. Mean R_a values for 316L, DSS 2205 and 254 SMO were 0.4785 µm, 0.4517 µm and 0.4975 µm respectively. The target was to keep all samples below the critical threshold of $R_a < 0.8$ µm, established for food-grade solutions in contact with metal surfaces [59]. Samples exceeding this threshold were re-ground in the following batch. Optical microscopy revealed that the number of rejected samples for DSS 2205 was more than double that of 316L and 254 SMO, which is consistent with the poor grindability of DSS 2205 reported in the literature, where higher R_a values, porosity and surface defects are commonly observed after grinding [35]. An example of a grinded sample without welding is displayed in Figure 9 a).

Following surface preparation, samples were immersed in 70% (v/v) ethanol and subjected to ultrasonic cleaning for 5 minutes, then carefully removed, dried in air or with compressed air, and stored in closed containers for a minimum of 7 days to allow natural oxidation. Prior to testing, samples were cleaned with water and ethanol and dried before being mounted in the test chamber and secured with a screw. The exposed metal surface area in the test chamber defined by the O-ring may vary due to temperature-induced perturbations [5] or compression of the O-ring when tightening the screw.

3.2.2 Sample preparation of welded 254 SMO SS

The 254 SMO samples used in this study were cut and welded by autogenous PC-GTAW without filler material and without shielding gas, by an internal supplier at Tetra Pak. Samples were cut to variable lengths with a diameter of 12 mm. The welding parameters used were a high current of 90 A, a low current of 30 A, and a pulse rate of 0.2 to 0.25 Hz. A single weld line was applied approximately through the center of the sample surface.

No grinding was applied to the sample surface before or after welding. Surface roughness (R_a) measurements showed that the WM zone had the highest roughness with large local variations, the HAZ had intermediate roughness still elevated by thermal effects, and the BM had the lowest values, below 1 µm. After preparation, all samples were cleaned with 70% (v/v) ethanol to remove surface residues before being introduced into the test chamber. An example of a welded sample without grinding is displayed in Figure 9 b).

(a) (b)

Figure 9: *(a) Example of base SS grinded sample without welding. (b) Example of a 254 SMO SS sample after welding, without any grinding treatment applied.*

3.3 Material Grades and Chemical Composition

Table 1 presents the chemical compositions of the three stainless steel grades used in this study, 316L (EN 1.4401), 2205 Duplex (EN 1.4462), and 254 SMO (EN 1.4547), as supplied by an internal Tetra Pak supplier, along with the composition ranges reported in the literature [60, 61, 62]. Since the supplier values fall within the literature ranges, a meaningful comparison between grades can be made.

Table 1: *Chemical composition of the grades (wt%) used: 316L SS, 2205 DSS and 254 SMO SS.*

Grade	Source	Cr	Ni	Mo	Mn	Si	N	P	C	S	Other elements
316L SS	Supplier	16.71	10.15	2.06	1.52	0.48	0.06	0.031	0.016	0.025	Co = 0.144
	Standard	16-18	10-14	2-3	2.0	0.75	0.1	0.045	0.03	0.03	-
2205	Supplier	22.34	5.1	3.22	1.6	0.44	0.171	0.026	0.018	0.002	-
DSS	Standard	22.0-23.0	4.5-6.5	3.0-3.5	2.00	1.00	0.14-0.2	0.03	0.03	0.02	-
254	Supplier	20.17	18.17	6.09	0.92	0.50	0.20	0.028	0.014	0.001	Cu = 0.74; W = 0.022
SMO SS	Standard	19.5-20.5	17.5-18.5	6.0-6.5	1.0	-	0.18-0.22	-	0.02	-	Cu = 0.5-1.0

Looking at the compositions, 316L stands out for having the lowest levels of Cr and Mo, along with relatively modest Ni content. 2205 Duplex shows higher amounts of both Cr and Mo, as well as a greater proportion of N. 254 SMO, on the other hand, reflects its superior corrosion resistance through a notably high Mo content, nearly three times that of 316L, combined with elevated Cr levels. Small additions of Cu and W are also present, further contributing to its corrosion resistance.

Using the PREN indicator introduced in the theoretical framework before in Section 2.2, values were calculated from these compositions: 24.46 for 316L, 35.7 for 2205 Duplex, and 43.5 for 254 SMO. These figures reflect the pitting corrosion resistance ranking of each grade, where a higher PREN indicates better pitting corrosion resistance, and serves as a useful baseline for interpreting the results of this study and guiding the selection of an appropriate stainless-steel grade.

3.4 Electrochemical setup for CPDP

For CPDP measurements, Autolab PGSTAT101 potentiostat was used, connected to an Ag/AgCl reference electrode, a glassy carbon counter electrode, and the SS sample as the working electrode within the test chamber (Figure 3). The software NOVA 2.1.8 was used to control the potentiostat via a USB interface. This software was configured to first measure the open circuit potential (OCP) for 30 minutes, followed by the CPDP scan. The CPDP scan started at −0.2 V vs OCP to provide a small safety margin below the rest potential, with a scan rate of 1 mV/s and a step size of 1 mV, in accordance with ASTM standards [5].

Before each experiment, a 7 mm internal diameter O-ring was placed in the test chamber, leaving an exposed sample surface area of 0.385 cm^2. The SS sample was then inserted and secured with a screw. The reference electrode was positioned approximately 4 mm from the sample surface.

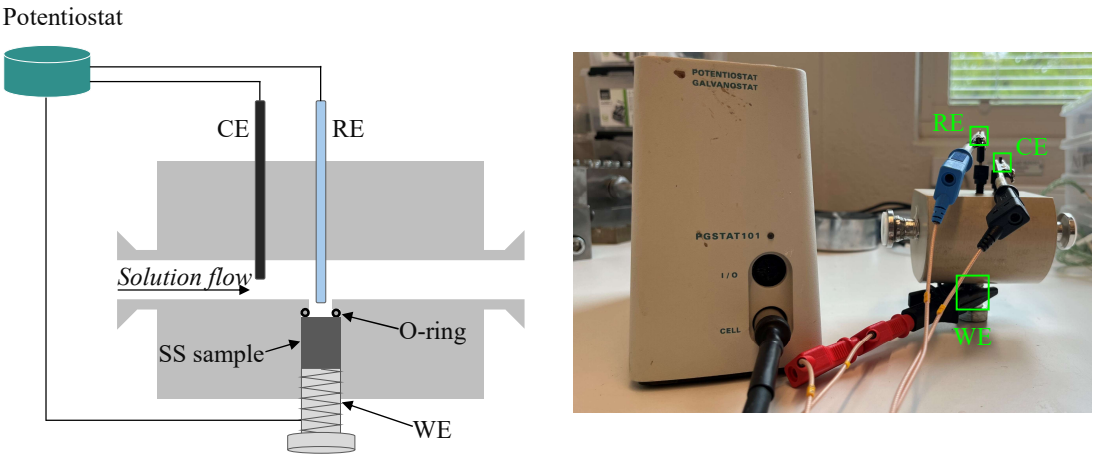

Figure 10: *Potentiostat connected to test chamber using a three-electrode cell configuration. (a) Schematic illustration. Potentiostat applies and controls the potential between the metal (WE) and RE. The resulting current is measured between CE and WE. (b) Image of potentiostat (left) connected to electrodes (right). Cables are attached through clip cables: RE (blue), CE (black) and WE (black).*

A lower potential limit of −0.55 V vs Ag/AgCl was set to prevent hydrogen evolution [5]. The upper vertex potential (E_v) was set to avoid oxygen evolution: 0.7 V for 316L, 1.5 V for 2205 Duplex, and 2.0 V for 254 SMO. The higher limits set for the two higher SS alloys is due to their superior corrosion resistance, where in certain conditions, these grades can reach higher potentials without undergoing pitting before the scan reverses. It is important to note that at potentials around 0.7 V and above, transpassive dissolution of the passive oxide layer and oxygen evolution may occur simultaneously, and this requires careful consideration when interpreting results. An additional upper limit of i_t=5 mA/cm² (equivalent to 1.925 mA for the exposed area) was applied in accordance with ASTM standards [5]. The reverse scan was triggered upon reaching either E_v or the current density limit, and stopped when it intersected the forward scan (E_{prot}) or reached −0.2 V vs OCP. The flow rate during all experiments was 1.13 L/min, corresponding to a pump frequency of 30.1 Hz on the Sören control panel.

After each experiment, the solution was drained through the valve after the feed tank, and water was flushed through the system for 5–10 minutes (or 30 minutes for a more thorough clean, performed periodically rather than between every experiment). Electrodes and the O-ring were cleaned after each run.

3.5 Electrolyte Composition

Each experiment used 2 L of solution, which were mixed before manually with a stirring rod and then loaded directly into the feed tank. Chloride-containing solutions were prepared using commercial fine non-iodised salt (*Finkornigt salt*), consisting of 99.8 wt% NaCl and 0.2 wt% anti-caking agent (E535/E536). To reduce pH, commercial vinegar (*Ättika 24%*) was used, containing 24 wt% acetic acid (E260) and 76 wt% water. The water content of the vinegar was accounted for when calculating solution concentrations.

3.6 Software tools for Analysis

Data obtained from NOVA 2.1.8 was analyzed in MATLAB using the Statistics and Machine Learning Toolbox. Normality was assessed through the Anderson-Darling test (*adtest*) for both the OCP–E_{corr} difference and the E_{pit} values, with normal probability plots generated using *normplot*. Standard deviations were computed with the *std* function.

The relative contribution and statistical significance of each factor (SS grade, Cl^- concentration, temperature and AcOH), both individually and in combination, were evaluated by multifactor ANOVA (*anovan*). Tukey's HSD post-hoc test (*multcompare*) was then used to identify significant pairwise differences within SS grades. Additional functions such as *Interp2* were used for point estimation among known data. The *surf* function was used to plot 3D surfaces and *smoothdata* for curve smoothing.

4. Results

4.1 General Electromechanical Behavior (OCP)

4.1.1 OCP Measurements

OCP was measured prior to CPDP for all three materials across every experiment (77 experiments). The results showed in a consistent way that elevated temperatures and high chloride concentrations are the two dominant factors shifting OCP towards more active potentials in all cases. The following mean values of OCP can be seen in Appendix A.2. At 30°C with 0.1% Cl^-, all three stainless steels reach their most noble mean OCP values, with +0.278 V for 316L, +0.346 V for 254 SMO and +0.383 V for Duplex, indicating a well-formed and stable passive oxide layer. At the opposite extreme, at 90°C with 3% Cl^- and no AcOH, all three materials register their lowest OCP values: −0.174 V for 316L, −0.155 V for Duplex and −0.090 V for 254 SMO, reflecting a passive layer significantly compromised by the combined effect of high temperature and high chloride concentration. The approximately 0.5 V range between the most and least aggressive conditions represents the shift in the natural corrosion potential of each material, driven by accelerated oxide dissolution at high temperatures [63] and increased passive layer degradation at high chloride concentrations [64]. As a first observation, this pattern suggests that 254 SMO exhibits superior pitting resistance compared to 2205 Duplex, which in turn outperforms 316L, as is expected from the theory.

Temperature and chloride concentration act as the two dominant factors, reducing mean OCP by 0.2 to 0.3 V when going from 30°C to 90°C, with high chloride concentration producing additional shifts of similar magnitude.

The effect of AcOH is secondary and less systematic. In most conditions for 316L and Duplex, its presence shifts OCP slightly towards more active potentials by no more than 50 mV, suggesting that acetate mildly acidifies the solution and increases the aggressiveness of the metal-solution interface, though to a much lesser extent than temperature or chloride concentration. However, this behaviour is not consistent across all conditions. An exception is observed in 254 SMO, where AcOH shifts OCP towards more noble values at 90°C, from −0.090 V to −0.025 V with 3% Cl^- and from −0.009 V to +0.125 V with 0.1% Cl^-. This opposite response could suggest that something specific in the composition of 254 SMO, could interact with acetate differently than in 316L and 2205 Duplex.

4.1.2 OCP/E_{corr} discrepancy

The analysis is based on 77 experimental measurements across three SS under different combinations of temperature, chloride concentration and acetic acid addition. Of these, 58 had a complete OCP-E_{corr} pair, as in 19 cases E_{corr} could not be recorded during the CPDP sweep. The variable studied is $\Delta E = OCP - E_{corr}$, which determines how much the open circuit potential deviates from the corrosion potential extracted from the polarization curve. Although theoretically both values should be similar, in practice this is not always the case.

Figure 11 shows each of the 58 complete pairs as a single point distinguished by material. The dashed lines mark the ±0.05 V tolerance threshold. Most points lie above the upper limit (in absolute values): 72.4% of samples exceed that threshold, suggesting OCP and E_{corr} may not be directly interchangeable. The OCP tends to be slightly more noble than E_{corr}, with a mean ΔE of +0.053 V and a standard deviation of 0.109 V. The considerable scatter reflects the heterogeneous nature of the metal-electrolyte interface, particularly in the presence of Cl^- and AcOH, which attack the passive oxide layer in a localized and unpredictable manner. A one-sample t-test against zero gives $p = 4.78\times10^{-4}$, confirming the discrepancy could be real and systematic. As suggestion to this could be those 30 minutes of OCP stabilization is insufficient under dynamic flow conditions, where flow modifies interfacial kinetics and continuously alters the passive oxide layer.

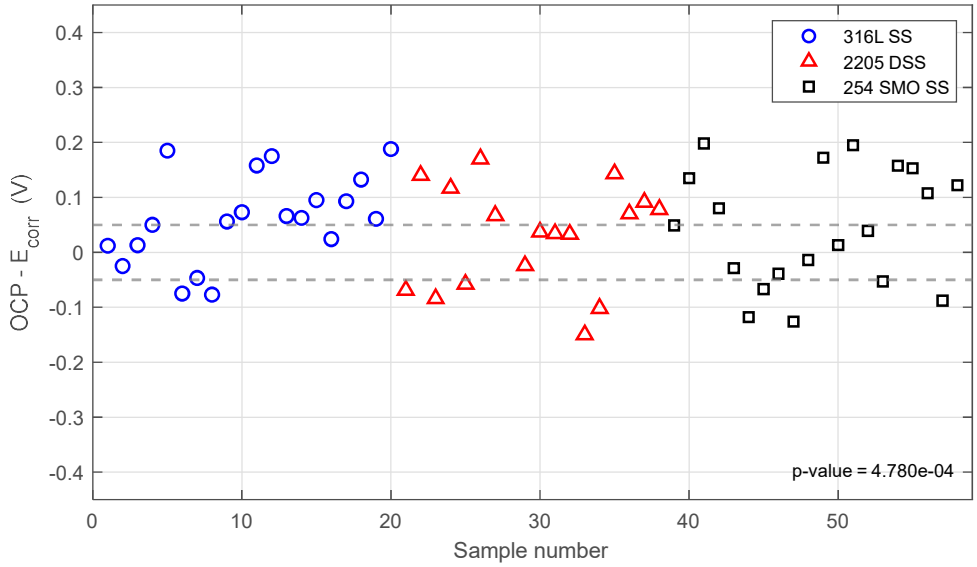

Figure 11: *All OCP – E_{corr} distinguished by SS grade with a mean ΔE of +0.053 V and a standard deviation of 0.109V.*

The Anderson-Darling test confirmed normality (h = 0, p = 0.314), justifying the use of parametric ANOVA models. The first ANOVA model considered the four main effects independently. None was significant at α = 0.05, with the error sum of squares clearly dominating, meaning most variability in ΔE is not explained by any single factor. The closest result was Cl^- with p = 0.069. Interestingly, the 0.1% Cl^- group shows a higher mean ΔE (+0.076 V) than the 3% Cl^- group (+0.021 V). A possible explanation is that at high chloride concentrations the system evolves rapidly during the sweep, with E_{corr} already reflecting active dissolution and converging towards OCP, whereas at low chloride concentrations the passive film responds more slowly and the gap between both measurements remains larger. The absence of a material effect suggests the discrepancy is driven more by measurement kinetics than by the specific alloy. The Anderson-Darling test and the ANOVA tables can be seen in Appendix A.3.

The second ANOVA model introduced three physically motivated interactions: Grade×Cl^-, Grade×Temp and Cl^-×AcOH. The Cl^-×AcOH interaction was the only significant result, with p = 0.038. When evaluated independently neither agent produces a significant effect, but their combination does, suggesting a synergistic action on the passive film. AcOH degrades the oxide layer and in the presence of chlorides amplifies their aggressiveness, promoting pit initiation and altering the interfacial kinetics between both measurements. To further explore a potential material-specific AcOH effect observed before in 254 SMO, an additional exploratory model including Grade×AcOH was run. This interaction was not significant (p = 0.286), while Cl^-×AcOH remained significant (p = 0.039), suggesting robustness across model structures. Tukey HSD post-hoc comparisons confirmed no individual pair of levels within any factor differed significantly.

In summary, the OCP-E_{corr} discrepancy could be real and systematic, but not controlled by any single variable independently. The only consistent signal is the joint action of Cl^- and AcOH, suggesting that when both are present simultaneously the interfacial evolution between measurements is particularly unstable and 30 minutes of stabilization is likely insufficient.

4.2 Interpretation of Polarization Curves

Before discussing the results more in detail, it is useful to introduce three phenomena that appeared frequently throughout the experiments and that are interesting for interpreting the polarization curves correctly: crevice corrosion, transpassive dissolution, and in the case of DSS 2205 and 254 SMO, a double passive region. Understanding this helps avoid misinterpreting what the curves were actually showing in the analysis, but also to make a righter, more detailed and far-reaching conclusions. The "*smoothdata*" function was applied in MATLAB (Figures 12, 13, and 15) to reduce signal noise and improve curve visualization.

The first general observation is that the electrochemical behaviour differed considerably between grades (Figure 13). For 316L, the passive film broke down at relatively accessible potentials (lower than 0.7 V) and the resulting current increase was consistently attributable to localized corrosion, allowing E_{pit} to be identified across all experiments. For DSS 2205 and 254 SMO, the passive film proved far more resistant and, in several conditions (medium-low aggressive), did not break down within the measurable potential window at all. What appeared instead was transpassive dissolution and oxygen evolution, a mix of processes that produce a current increase visually similar to pitting but physically distinct, since no actual pits form. This distinction between SS grades is important and runs through much of the discussion that follows.

4.2.1 Crevice Corrosion Phenomenon

Crevice corrosion proved to be one challenge in this project, but also an opportunity to have a better understanding of this phenomenon across the SS grades, since it is one of the most difficult localized corrosion types to tackle in reality. Its possible occurrence has already been mentioned in previous work using the same experimental setup [4, 5], and during these studies most pits were found beneath the O-ring rather than on the open metal surface. This raised the question of whether what was being measured was pitting, crevice corrosion, or a combination of both.

In the polarization curves, crevice corrosion can be observed as a slow and progressive increase in current density (Figure 12). The restricted geometry beneath the O-ring limits oxygen replenishment and promotes local acidification through hydrolysis [65], causing the passive film to deteriorate gradually rather than rupture suddenly. This gradual nature made it difficult to identify a clean sharp current event (E_{pit}) when crevice corrosion was present.

The degree to which this affected the results depended strongly on the SS grade. For 316L, crevice corrosion was often observed, particularly at low Cl^- concentrations (0.1%) and low temperatures (30°C), where it frequently masked any pitting signal and made E_{pit} difficult to determine. At 90°C with 0.1% Cl^- the gradual current rise was still visible, though somewhat less severe. In most of these conditions the backward scan showed $E_{prot} < E_{corr}$, indicating difficulty in repassivating, which according to some studies could itself serve as confirmation that crevice corrosion was occurring [66].

For DSS 2205 and 254 SMO the situation was quite different. Crevice corrosion was present to some degree but much less dominant, allowing pitting to remain the primary event and therefore, E_{pit} to be identified more clearly. Both grades behaved similarly to each other in this respect despite the higher PREN of 254 SMO, which could suggest that the level of resistance needed to suppress crevice corrosion under these conditions is already provided by DSS 2205. However, for these two high alloy SS grades, this gradual increase in current was more difficult to observe, and that raises the question of whether it was actually been measured crevice or not for these grades.

An example of the degree of dependence of crevice corrosion occurrence on the SS grade under mild conditions (90ºC with 0.1% Cl^-), is illustrated in Figure 12. Starting from E_{corr}, it can be observed that 316L has already the lowest of the three, at around −0.3 V, and the gradual current rise characteristic of crevice dominates its curve. Thus, making it difficult to observe and determine this sharp current density (E_{pit}). DSS 2205 and 254 SMO show a much cleaner passive region before any breakdown event. Some studies have determined the Critical Crevice Temperature (CCT), which is the temperature limit at which crevices appear under specific conditions. Determining the CCT for each grade in future work would help clarify the actual extent of crevice corrosion in this setup, particularly for the two higher-alloy grades where its presence was harder to confirm.

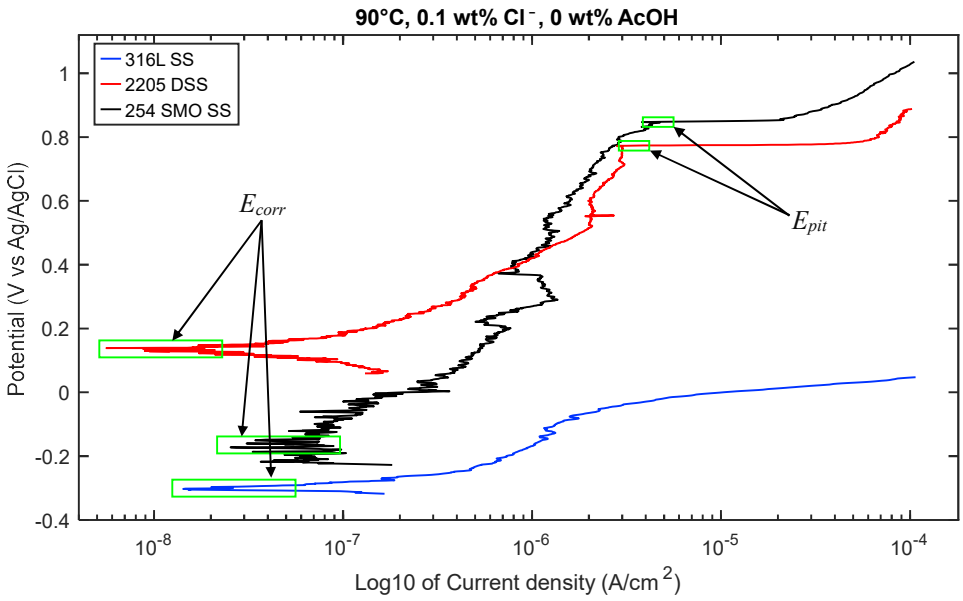

Figure 12: *Example of CPDP curves at 90°C, 0.1% Cl^- and 0% AcOH, showing E_{corr} for each grade of SS. A clean sharp current increase determines E_{pit} for 2205 Duplex and 254 SMO, while 316L shows a gradual increase in current, indicating crevice corrosion behavior and preventing the determination of pitting rupture.*

4.2.2 Distinction between E_{pit} and Transpassive Breakdown

This was possibly the most challenging aspect of the analysis, and it affected DSS 2205 and 254 SMO far more than 316L. For 316L the interpretation of localized corrosion was relatively straightforward, since a sudden and sustained current increase in the passive region reliably indicates passive film rupture (E_{pit}) and therefore localized corrosion [67]. For the higher-alloy grades, however, the same visual feature can have a different origin. Above a certain potential, chromium in the passive film oxidizes from Cr(III) to Cr(VI) and dissolves into solution (transpassive dissolution), which produces a current increase that looks almost identical to pitting in the curve even though no pits form, and thus, cannot be classified as localized corrosion [67].

This distinction could be partly linked to a concept investigated in several studies, known as Critical Pitting Temperature (CPT), which is a function of the material properties and chemical conditions that act as a threshold and served to interpret better when localized corrosion was actually been measured. Below this CPT, SSs tend to undergo transpassive dissolution rather than stable pitting. In previous studies for 254 SMO, the CPT has been reported at around 89°C in 4% NaCl [37], meaning that at 30°C and 0.1% Cl^-, the conditions used here, are well below this value and a transpassive response is what would be expected. Although the conditions differ from those of this project, they served as a useful guideline for the analysis.

To determine whether the sharp increase in current density corresponds to pitting corrosion initiation (E_{pit}) or transpassive dissolution, a two-criterion decision rule was applied throughout. The current increase was only classified as E_{pit} if it showed both: (1) a sudden and sustained rise within the passive region and (2) hysteresis in the backward scan. If either criterion was absent, the event was not attributed to pitting, but breakdown potential, denoted as E_{break}, which a neutral term used when there is ambiguity as to whether it is pitting corrosion or transpassive breakdown.

This approach is in line with previous work using the same setup, where 1.2 V vs Ag/AgCl was established as a rough upper threshold for distinguishing pitting from transpassive events [4], and with studies confirming through post-CPDP SEM that no pits formed on sample surfaces during transpassivation at high potentials [68, 69]. Therefore, in this study events occurring between 1.0 and 1.2 V were evaluated individually on a curve-by-curve basis.

The experiments where no clean E_{pit} (i.e. E_{break}) could be identified were not treated as inconclusive or discarded. The fact that DSS 2205 and 254 SMO did not exhibit pitting before reaching the transpassive region under several conditions is itself a meaningful result, confirming their high resistance to localized corrosion under those

environments [37]. The comparison with 316L, which consistently pitted at much lower potentials under the same conditions, remains valid and informative.

Figure 13 provides an illustration of this challenge, under conditions of 30ºC, 3% Cl^- and 3% AcOH, where for (a) 316L the sudden and sustained current increase at low potentials (<0.2 V) is attributed to E_{pit}, while for (b) DSS 2205 and 254 SMO this current increase occurs at relatively high potentials (0.9 V and 1.2 V), placing the events in the region where chromium oxide is unstable and thus, the question arises as to whether there is localized corrosion or transpassive breakdown and oxygen evolution have been reached.

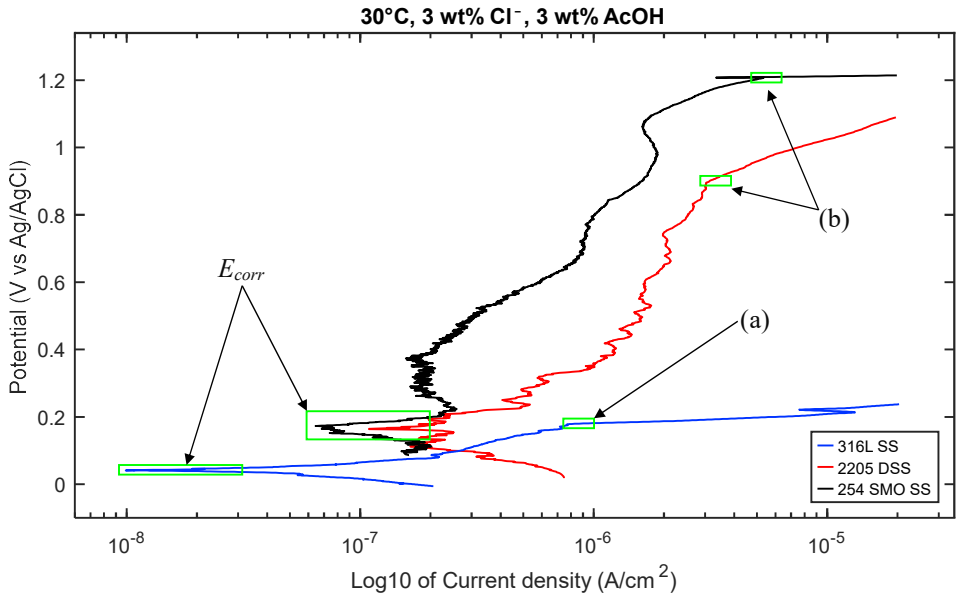

Figure 13: *CPDP curves at 30°C, 3% Cl^- and 3% AcOH for each grade. (a) The sharp current increase for 316L indicates clear pitting corrosion (E_{pit}). (b) For 2205 Duplex and 254 SMO the current increase is at higher potentials which could be determined by transpassive dissolution and oxygen evolution, instead by pitting corrosion. E_{corr} is shown as well.*

4.2.3 Double Passive Region in DSS 2205 and 254 SMO

One feature during CPDP experiments that did not appear in any of the 316L curves, was a polarization curve exhibiting two distinct passive regions, as shown in Figure 14. This was recorded for DSS 2205 at 30°C, 0.1% Cl^- and 0% AcOH, while not always as clearly defined, a similar pattern was observed in other DSS 2205 and 254 SMO experiments under different conditions. The same behaviour has been reported in the literature for both grades [71, 72] and for other stainless-steel alloys such as AM355 [70], so it is a recognized feature rather than an anomaly specific to this setup.

Four regions can be identified in Figure 14. A primary passive region (1) extends from approximately 0.33 V to 0.67 V vs Ag/AgCl, where the passive film is stable and current remains low. This is followed by an anodic peak (2) between 0.67 V and 0.89 V, attributed to the oxidation of Cr(III) to Cr(VI) within the passive film, which is transpassive dissolution rather than localized corrosion [70]. Beyond this point, instead of a continued current rise, a secondary passive region forms (3) between 0.89 V and 1.32 V. This secondary film is iron rich, forming as chromium dissolves away from the surface, and is structurally weaker than the primary layer due to a higher density of oxygen vacancies, though it does temporarily stabilize the current [70]. Above 1.32 V a final current increase (4) appears, attributed to a combination of oxygen evolution and further passive film breakdown [70, 72].

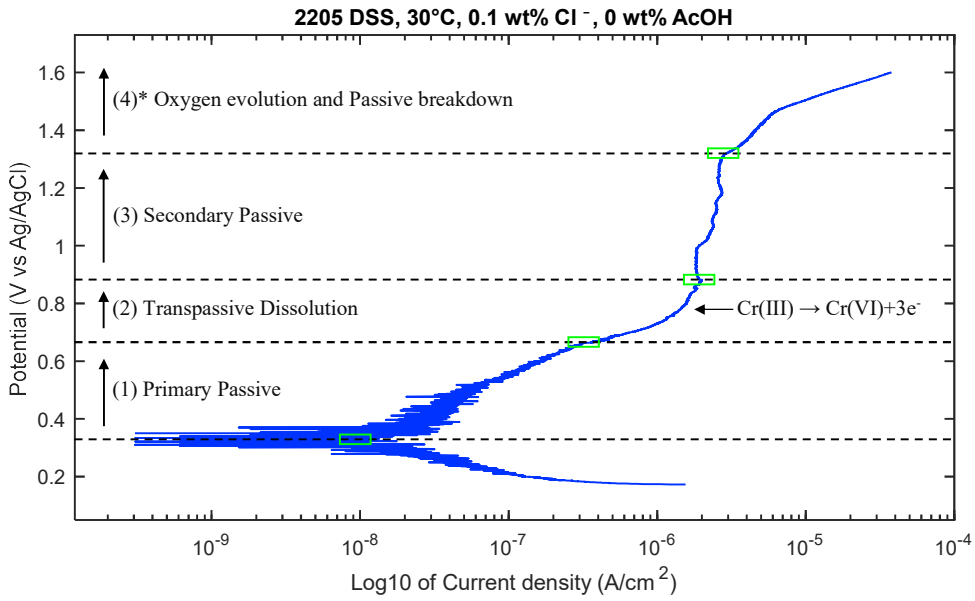

Figure 14: *Dual passive region for 2205 Duplex at 30°C, 0.1% Cl^- and 0% AcOH. The curve displays (1) a primary passive region, followed by (2) transpasisve dissolution. Then, (3) a secondary passive region, weaker than the first one is exhibited followed by (4) a current increase attributed to transpassive dissolution and oxygen evolution.*

The absence of hysteresis in the backward scan for these curves strongly suggested that no localized corrosion occurred, which is consistent with SEM studies in the literature that confirmed no pit formation after similar tests that exhibit two passivation regions [73].

4.2.4 Repassivation Behaviour

Once E_{pit} was reached, the capacity of each grade to repassivate was assessed through the hysteresis in the backward scan, specifically whether E_{prot} fell above or below E_{corr}. The results are broadly consistent with the expected corrosion resistance ranking of the three grades.

For 316L, hysteresis was recorded across all experiments and in 84% of cases E_{prot} was below E_{corr}, indicating that once pitting initiated, the passive film struggled to recover. This was particularly consistent at 90°C regardless of Cl^- concentration, which suggested that temperature may have a stronger effect than Cl^- concentration within the conditions of this project. For DSS 2205 and 254 SMO, the backward scan was only completed for one replicate per condition due to time constraints, as these grades reach considerably higher potentials before breakdown, making the full measurement significantly more time-consuming. Of the cases evaluated, DSS 2205 showed only one instance where $E_{prot} < E_{corr}$ (at 90°C, 0.1% Cl^-, no AcOH), and 254 SMO showed none. Therefore, the consistent positive E_{prot}-E_{corr} in almost all cases for high-alloy SSs indicated improved repassivation compared to 316L.

These results are consistent with the PREN differences between the three grades. However, the limited number of backward scans for DSS 2205 and 254 SMO reduces the statistical representativeness of this comparison, and future work should aim to complete the full hysteresis measurement across all conditions. It is also worth mentioning that $E_{prot} > E_{corr}$ does not guarantee that pitting will stop propagating once its formed, just as $E_{prot} < E_{corr}$ does not confirm that active pitting is ongoing [56]. Post-CPDP SEM would provide more direct evidence of the actual surface state after testing.

4.2.5 Variability in DSS 2205

In this study, a higher level of variability in DDS 2205 was observed across the three SS grades, which agrees with the previous literature in section 2.2.2. Specifically, a phenomenon related to this variability was observed between replicates within the same experiment. An example suggesting this event is shown in Figure 15, which displays three replicates at 30°C, 0.1% Cl^- and 3% AcOH. It can be seen highlighted an anodic dissolution peak for both (a) Tests 51 and 52, which show higher current density at lower potentials, while the highlighted dissolution peak for (b) Test 50 displays a more stable response at higher potentials.

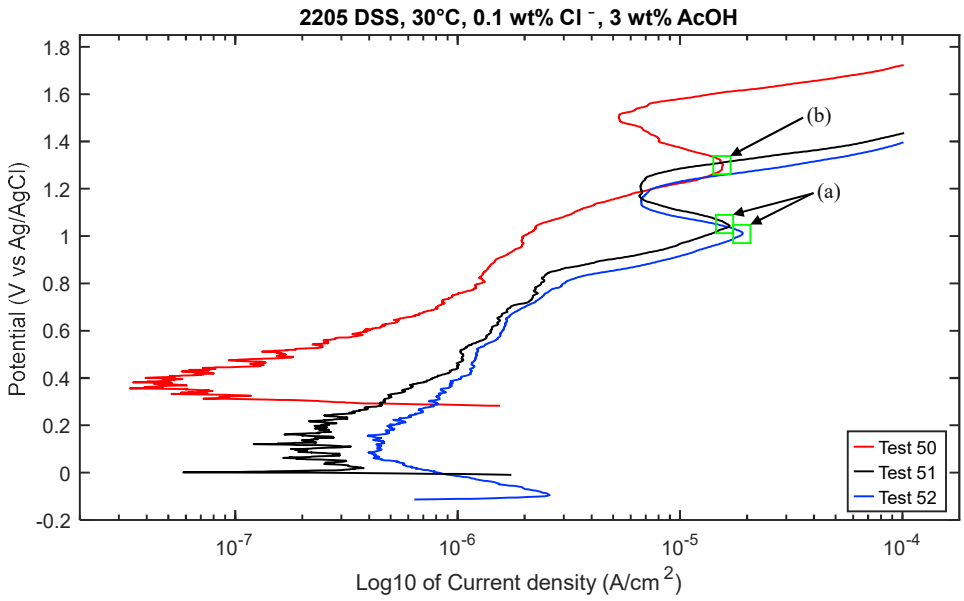

Figure 15: *Variability of 2205 Duplex between samples during CPDP. (a) Anodic dissolution peak occurs at lower potentials, which could be attributed to higher electrochemical activity at the ferrite phase (α). (2) Anodic peak occurs at higher potentials, which could be attributed to a more stable response at the austenite phase (γ).*

A possible explanation lies in the dual-phase microstructure of DSS 2205. The ferritic and austenitic phases respond differently to electrochemical perturbation, where ferrite (α), richer in Cr and Mo, is more electrochemically active and its anodic dissolution peak tends to occur at lower potentials, while austenite (γ), richer in Ni and N, is more stable and repassivates more readily [74]. Since the experimental setup in this project records the combined response of both phases simultaneously, the relative surface area of each phase exposed after grinding when doing the sample preparation can vary between replicates, shifting the overall curve towards a more active or more stable response. Therefore, Tests 51 and 52 would in this interpretation reflect surfaces with greater ferritic (α) exposure, while Test 50 could reflect one where austenite (γ) is more dominant.

Therefore, the variability observed in E_{pit} for DSS 2205 could suggest that, despite the nominal 50:50 phase fraction of the alloy, the electrochemical response is largely governed by which phase dominates the surface after sample preparation. Depending on whether ferrite or austenite is more exposed at the ground surface, the material will exhibit a more active response with lower E_{pit} values, or a more stable one with higher E_{pit} values. One way to confirm this interpretation would require measuring the electrochemical response of each phase independently, for example through a micro-electrochemical cell [74], which could be a worthwhile direction for future work.

4.3 Electrochemical behaviour of the SS grades

Before presenting the pitting corrosion results, it is worth clarifying again that for 316L, passive film breakdown consistently resulted in stable pit propagation, so the term E_{pit} was used throughout. For 2205 Duplex and 254 SMO, some conditions produced a sharp current increase attributable to transpassive dissolution rather than localized corrosion. In those cases, the term E_{break} was used instead of E_{pit}, acknowledging that the measured potential does not necessarily correspond to pitting initiation. The distinction between the two was discussed in detail in the variability analysis below (Section 4.3.5).

The most consistent pattern across all experimental conditions was the clear corrosion resistance hierarchy: 254 SMO > DSS 2205 > 316L, observed in Figure 16, that displays all mean E_{pit}/E_{break} values for each grade. This ranking holds without exception across every combination of temperature, chloride concentration and acetic acid content, and is directly consistent with the PREN values calculated earlier for each grade. One example that illustrates it, is under mild conditions, such as 30°C and 0.1% Cl^- without AcOH (shown in Figure 17), where the separation between grades is clearly visible, with mean E_{pit}/E_{break} values of 0.521 V for 316L, 1.338 V for DSS 2205 and 1.456 V for 254 SMO. As conditions become progressively more aggressive, E_{pit}/E_{break} values decrease for all three grades, but the ranking is preserved throughout. The gap between grades varies depending

on the condition, and in some cases the values of DSS 2205 and 254 SMO approach each other, but the hierarchy never reverses.

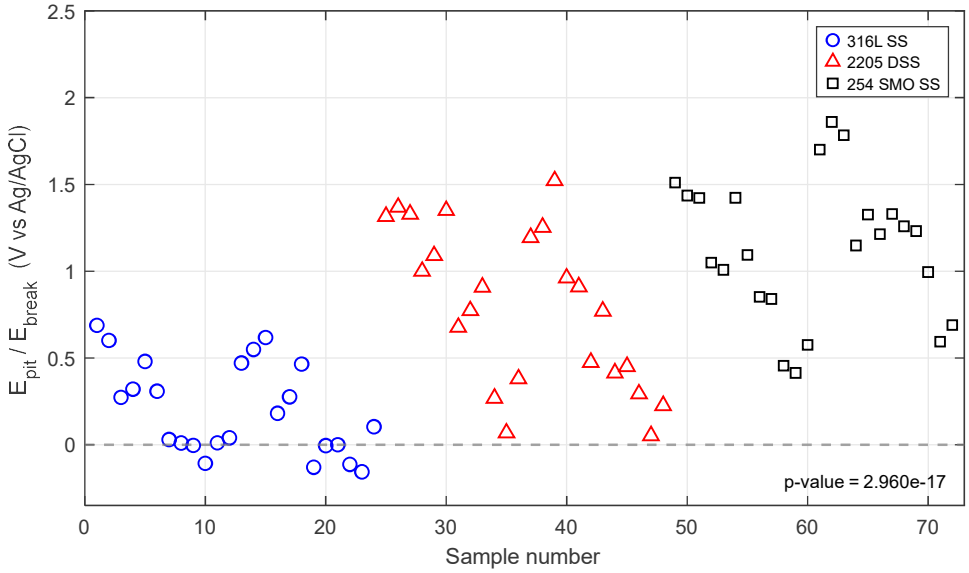

Figure 16: *All E_{pit} /E_{break} distinguished by grade. Values indicate that 254 SMO exhibits the highest corrosion resistance, followed by 2205 Duplex and then 316L, in accordance with their PREN values. Limited resistance of 316L for some conditions is given by their low and negative values for some conditions.*

4.3.1 Effect of temperature

Temperature is the most limiting factor on E_{pit} /E_{break} across the entire dataset (Figure 19). The drop from 30°C to 90°C is consistently large for all three grades, though its magnitude varies with grade and chloride concentration. Figure 17 and Figure 18 illustrate these trends as a function of Cl^- concentration and temperature respectively.

For 316L the effect of temperature is devastating. Without AcOH, E_{pit} drops from 0.521 V at 30°C to 0.012 V at 90°C at 0.1% Cl^-, and from 0.37 V to −0.019 V at 3% Cl^-. These near-zero and negative values indicate that at 90°C the passive oxide layer has already collapsed to a degree where neither chloride concentration nor AcOH content produces any meaningful additional effect. With AcOH the situation is equivalent, with values of −0.045 V and −0.055 V respectively at 90°C. Importantly, at 90°C the E_{pit} curves for 316L become nearly horizontal regardless of Cl^- or AcOH, confirming that temperature is the primary limiting factor for this grade and that once the passive film is thermally degraded to this extent, further changes in electrolyte composition add little further damage. This thermal saturation effect is a meaningful observation for material selection purposes, as it suggests that 316L becomes unreliable at elevated temperature regardless of the other processing parameters.

For DSS 2205 the temperature drop is most pronounced at 3% Cl^- without AcOH, where E_{break} falls from 1.147 V to 0.239 V, a reduction of 0.908 V. At 0.1% Cl^- the reduction is smaller at 0.552 V, suggesting a strong interaction between temperature and chloride concentration for this grade, consistent with the accelerated passive film dissolution kinetics reported at elevated temperatures [63]. With AcOH at 3% Cl^-, the temperature induced drop is somewhat smaller at 0.592 V, which can be explained by the fact that the E_{break} values at 30°C with AcOH are already lower due to the detrimental effect of acetic acid on this grade, leaving less room for further reduction.

For 254 SMO the temperature effect is comparatively more moderate in relative terms, but still significant. Without AcOH, E_{pit} /E_{break} drops by 0.527 V at 0.1% Cl^- and by 0.678 V at 3% Cl^-. Crucially, even under aggressive conditions such as 90°C and 3% Cl^- without AcOH, 254 SMO maintains an E_{pit} of 0.482 V, a value that reflects the superior pitting resistance of this grade and contrasts sharply with the negative E_{pit} values of 316L under identical conditions.

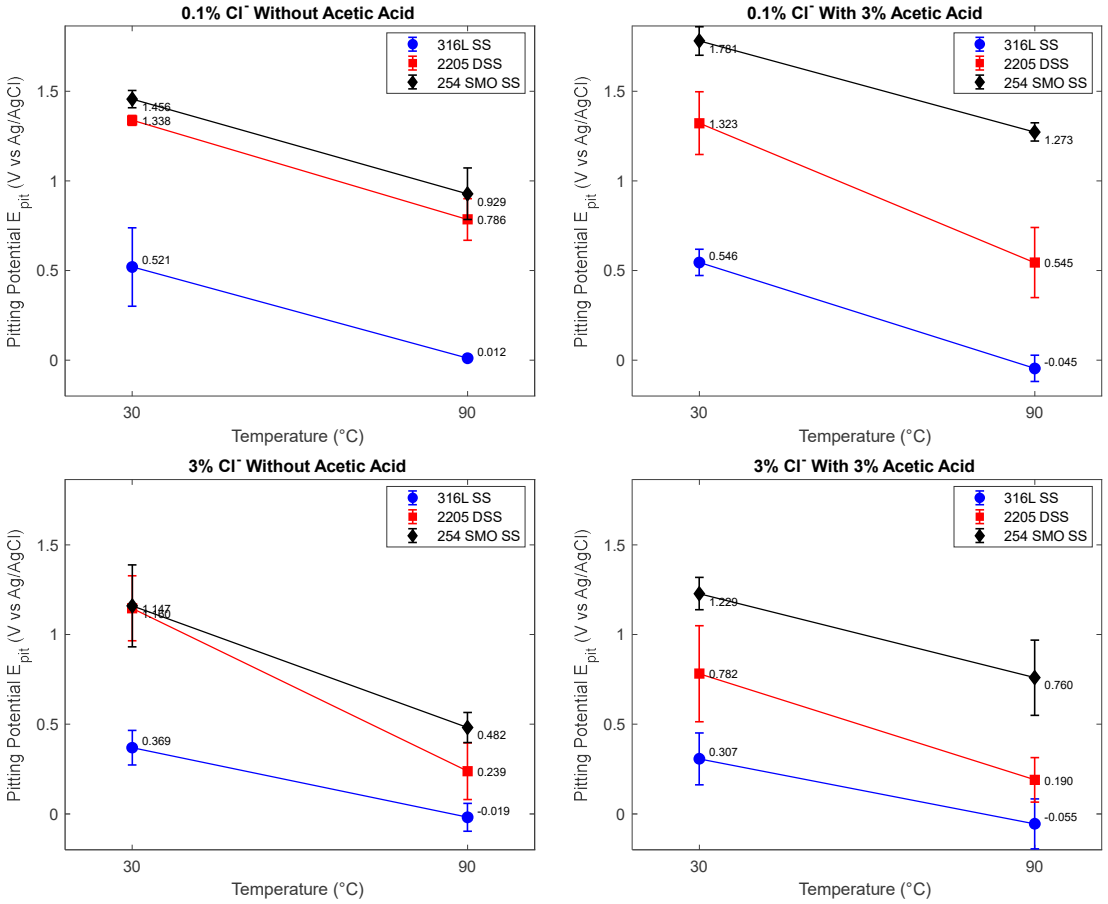

Figure 17: *Mean values of E_{pit} /E_{break} and their variability of each SS grade for different temperatures at Cl^- concentrations and with and without AcOH. Values attributed to transpassive dissolution (E_{break}) that did not exhibited pitting were also included.*

4.3.2 Effect of chloride concentration

Chloride concentration is the second most limiting factor on E_{pit} /E_{break} on this study. Increasing Cl^- from 0.1% to 3% consistently reduces E_{pit} /E_{break} across all grades and conditions, though the magnitude of this reduction depends strongly on temperature and grade.

For 316L at 30°C the reduction is moderate, approximately 0.15 V without AcOH and 0.24 V with AcOH. At 90°C, where E_{pit} is already close to zero, the additional drop due to chloride is very small, at most 0.03 V, because the passive oxide layer is already so thermally degraded that further chloride attack produces negligible additional damage. This again illustrates the dominance of temperature as the primary limiting factor for 316L.

For DSS 2205 the chloride effect is more pronounced at high temperature. The E_{break} drop at 30°C without AcOH is 0.19 V, while at 90°C it reaches 0.55 V. With AcOH at 30°C the drop is 0.54 V and at 90°C 0.36 V. This pattern suggests that elevated temperature significantly amplifies the sensitivity of DSS 2205 to chloride concentration, consistent with accelerated passive film dissolution kinetics at high temperature [63].

For 254 SMO a similar trend is observed. Without AcOH the drop from 0.1% to 3% Cl^- is 0.30 V at 30°C and 0.45 V at 90°C. With AcOH it is 0.55 V at 30°C and 0.51 V at 90°C. Notably, the standard deviations of E_{break} for 254 SMO with AcOH tend to be very low across both chloride concentrations and both temperatures, with the exception of the 90°C and 3% Cl^- condition. As discussed further in the variability section, this low scatter in conditions where E_{break} falls in the transpassive region, could be interpreted as signal of a more deterministic behaviour of transpassive dissolution compared to pitting corrosion.

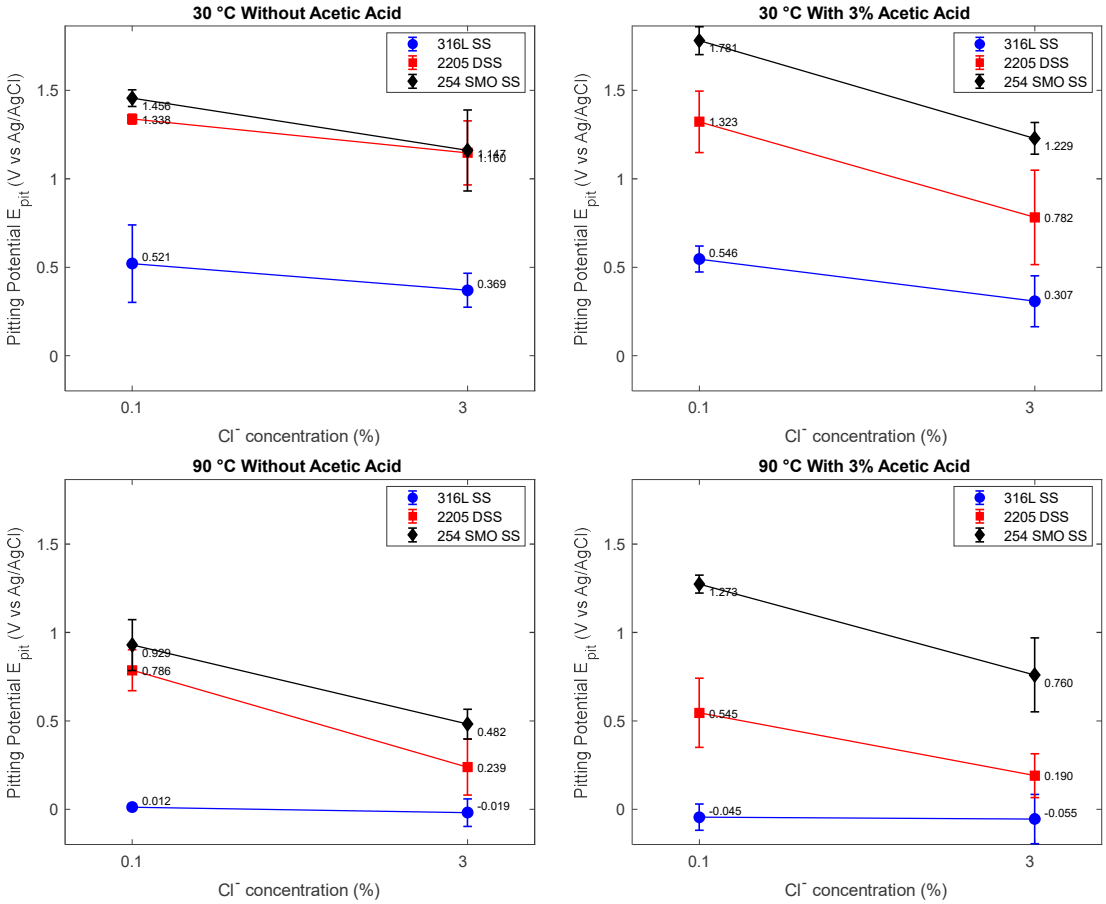

Figure 18: *Mean values of E_{pit} /E_{break} and their variability of each SS grade for different Cl^- concentrations at different temperatures and with and without AcOH. Values attributed to transpassive dissolution that did not exhibited pitting were included and are denoted as E_{break}.*

4.3.3 Effect of AcOH

The effect of acetic acid is without any doubt the most complex and most unexpected finding of this study, because it is not consistent between grades. Figure 19 illustrates this clear difference among the SS grades.

For 316L, AcOH generally produces a slight reduction in E_{pit}. The only apparent exception is at 30°C and 0.1% Cl^-, where the addition of AcOH produces a negligible increase of 0.025 V. However, this apparent increase is likely due to the high standard deviation without AcOH (0.22 V) caused by two replicates with E_{pit} above 0.6 V and one below 0.3 V, compared to the much tighter distribution with AcOH (standard deviation 0.074 V) where all three replicates were within 0.2 V of each other. The stochastic nature of pitting corrosion can produce this sort of between replicate variability. In all other conditions for 316L, AcOH reduces E_{pit} slightly, typically by less than 0.10 V.

For 2205 DSS, AcOH produces a more pronounced reduction in E_{break} than for 316L. The largest drops are observed at 30°C and 3% Cl^- (−0.365 V) and at 90°C and 0.1% Cl^- (−0.241 V). This suggests that the combination of AcOH with chloride can significantly reduce E_{break} in DSS 2205. The comparatively smaller relative effect in 316L could be explained as mentioned before by the thermal saturation effect described above, where at 90°C the passive oxide layer of 316L is already so weakened that the additional effect of AcOH has little further impact.

For 254 SMO the effect reverses completely and consistently. AcOH increases E_{pit} /E_{break} across all four conditions. At 30°C and 0.1% Cl^- the increase is +0.33 V (from 1.456 V to 1.781 V), at 90°C and 0.1% Cl^- it is +0.34 V (from 0.929 V to 1.273 V), at 30°C and 3% Cl^- it is +0.069 V, and at 90°C and 3% Cl^- it is +0.28 V. In all conditions, therefore, AcOH tends to show a protective or inhibitory effect for 254 SMO, and this effect is most pronounced at high temperature. This is also consistent with the OCP analysis done before, where for 254

SMO at elevated temperature, OCP values tended to be higher in the presence of AcOH, providing confirmation of the ennoblement effect.

The practical consequence of this AcOH effect on the comparison between DSS 2205 and 254 SMO is significant. Without AcOH, the difference in E_{pit}/E_{break} between the two grades ranges from 0.013 V to 0.143 V depending on condition. With the addition of AcOH, this difference widens to a range of 0.447 V to 0.728 V, meaning the advantage of 254 SMO over DSS 2205 is amplified by more than three times in the presence of acetic acid.

The mechanism responsible for this inhibitory effect in 254 SMO remains to be established. Two possible explanations are proposed. The first is that AcOH could block chloride ions at the passive film surface through competitive adsorption, with this blocking effect translating into higher E_{pit} only in 254 SMO whose passive film is sufficiently intact and robust to convert reduced Cl^- surface activity into measurably higher breakdown potential (E_{break}). The second could be an interaction between acetate species and the Mo-enriched passive film of 254 SMO. Previous work using the same experimental setup observed small inhibitory effects at very low Cl^- concentrations (10 ppm) with 3% AcOH for 316L [4], but the significantly larger and consistent effect observed here for 254 SMO across all conditions may suggest a mechanism specific to the alloy composition, particularly its high Mo and N content. Further investigation using complementary surface analytical techniques could be considered to confirm the precise mechanism.

4.3.4 Statistical analysis of factor effects

The statistical analysis was performed on a balanced dataset of 72 E_{pit}/E_{break} measurements, 3 replicates per condition, with no missing values. The Anderson-Darling normality test gave h=1 and p=0.023, rejecting normality at α=0.05. This is expected given that the dataset combines three grades with very different mean values, producing a multimodal distribution. However, ANOVA remains valid for a balanced design with equal group sizes.

ANOVA with main effects only (ANOVA 4) confirmed that Grade ($p=5.82\times10^{-25}$), Temperature ($p=1.95\times10^{-19}$) and Cl^- concentration ($p=7.55\times10^{-10}$) are all highly significant, while AcOH is not significant as a main effect (p=0.689). The sum of squares decomposition reveals the relative contribution of each factor to total E_{pit}/E_{break} variance: Grade accounts for 51.06%, Temperature for 28.34%, Cl^- for 9.03%, AcOH for 0.03%, and residual error for 11.54%.

ANOVA with interactions (ANOVA 5) added the interaction terms Grade×Cl^-, Grade×Temp, Grade×AcOH and Cl^-×Temp. Of these, Grade×Cl^-, Grade×Temp and Grade×AcOH were all significant, confirming that the effects of temperature, chloride and AcOH differ quantitatively between grades. The Grade×Temp interaction shows that the percentage reduction in mean E_{pit}/E_{break} from 30°C to 90°C is −106.1% for 316L, −61.7% for DSS 2205 and −38.8% for 254 SMO, confirming that 316L suffers disproportionately more thermal damage than the other two grades. The Grade×Cl^- interaction shows that the percentage reduction from 0.1% to 3% Cl^- is −41.7% for 316L, −40.9% for DSS 2205 and −33.3% for 254 SMO, relatively similar in proportional terms across grades but more visible in absolute terms for DSS 2205 and 254 SMO given their higher starting values. The Grade×AcOH interaction, added as an exploratory term motivated by the observation of opposite AcOH effects between grades, was highly significant ($p=1.29\times10^{-5}$), confirming that the effect of acetic acid on pitting resistance is grade dependent: −14.8% for 316L, −19.1% for DSS 2205 and +25.2% for 254 SMO. The Cl^-×Temp interaction was not significant, confirming that temperature and chloride act additively on E_{pit}/E_{break} without mutual amplification detectable at this sample size. The overall model explains 91.6% of total variance (R^2=0.916, R^2adj=0.902), confirming that the experimental factors dominate over measurement noise, in sharp contrast with the OCP−E_{corr} analysis where the adjusted R^2 was only 0.030. The Anderson-Darling test and the ANOVA tables can be seen in Appendix A.4.

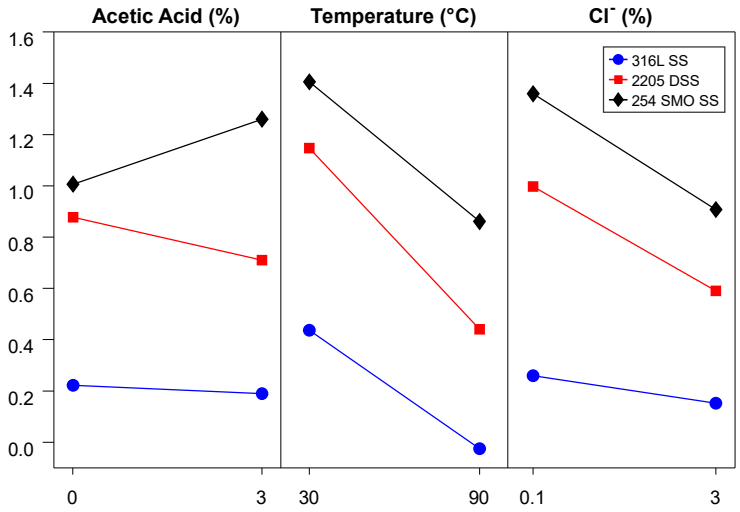

Figure 19: *Main effect of AcOH, temperature, Cl^- on each SS grade.*

4.3.5 Variability patterns across SS grades

The overall standard deviations across all conditions are 0.455 V for DSS 2205, 0.405 V for 254 SMO and 0.267 V for 316L (seen in Table 2). These differences reflect several distinct physical mechanisms mentioned in this analysis.

For 316L the relatively low overall standard deviation is strongly influenced by the thermal saturation effect at 90°C, where E_{pit} consistently falls to near-zero values across all replicates regardless of Cl^- or AcOH, leaving little room for between-replicate variation. At 30°C the passive oxide layer is more functional and the distribution of E_{pit} values is broader, reflecting the stochastic nature of pit initiation at sites such as MnS inclusions [75]. At 90°C and 3% Cl^- as mentioned before, however, a notable exception was observed, illustrating that even in highly degraded passive film conditions the stochastic nature of pitting cannot be completely suppressed.

For DSS 2205 the higher variability is consistent with its duplex microstructure. The ferritic and austenitic phases have different electrochemical responses as it was discussed before in section 4.2.5, where ferrite, enriched in Cr and Mo, could tend to experience lower E_{break} values, while austenite, enriched in Ni and N, could be more stable and repassivate easily. Since the experimental setup records the combined response of both phases, the relative surface area of each phase exposed after grinding varies between replicates, shifting the overall electrochemical response. Additionally, grain boundaries and ferrite-austenite (α/γ) interfaces represent preferential pitting initiation sites, and the greater number and variety of such initiation sites in 2205 DSS compared to the austenitic 316L contributes to its wider range of measured E_{pit}/E_{break} values. A clear example of this was observed at 30°C, 0.1% Cl^- and 3% AcOH for DSS 2205, where some replicates showed higher E_{break} values at lower current density while others showed lower E_{pit}/E_{break} at higher current density, which could be consistent with the electrochemical response being dominated by different phases depending on which was more exposed at the ground surface.

For 254 SMO a particular pattern emerged, which was that the standard deviation of E_{break} tends to be very small in conditions where values fall in the transpassive region or near the oxygen evolution potential. This low variability in high E_{break} conditions could be interpreted as a more deterministic behaviour of transpassive dissolution compared to pitting corrosion. This deterministic behavior could be controlled by thermodynamic boundaries in the Pourbaix diagram (mentioned before in Section 2.3.4), particularly within the Cr(III)/Cr(VI) oxidation zones and the oxygen evolution limits. In these regions, the electrochemical response is controlled by the passive layer as a whole, rather than by heterogeneities as seen in localized corrosion. Consequently, under the experimental conditions studied and especially pH, the E_{break} values that show low variability still shift slightly between conditions (Cl^-, temperature and pH) within these transpassive regions due to these thermodynamic boundaries that change when changing these conditions, while remaining within small variations. From a physical standpoint, the transition from passive to transpassive behaviour could correspond to a change in the electrochemical state of the passive film interface, specifically the transition from band-edge level pinning to Fermi-level pinning, which occurs at a relatively fixed potential and represents a general dissolution of the

passive oxide layer surface [76]. In contrast, pitting initiation depends on local events such as the distribution of inclusions, surface defects and microstructural heterogeneities, which vary more stochastically between replicates [75]. This intrinsic difference between the two mechanisms could explain why E_{break} values in the transpassive region show much lower scatter than E_{pit} values in conditions where localized corrosion dominates. The same pattern of low variability of E_{break} was observed in 2205 DSS, though less consistently, which is expected given its lower PREN and correspondingly less frequent occurrence of transpassive conditions within the experimental range. The observation that adding AcOH to 254 SMO in some conditions shifted potentials from the pitting region to the transpassive region, with a reduction in standard deviation, provides additional indirect evidence for an inhibitory behaviour of AcOH in this grade, that should be studied in future work.

Table 2: *Mean values of E_{pit} /E_{break} and their variability for each SS grade.*

Factor	Mean E_{pit}/E_{break} (V)	Standard deviation (V)
316L SS	+0.2046	0.2672
2205 DSS	+0.7937	0.4549
254 SMO SS	+1.1338	0.4046
30ºC	+0.9967	0.4801
90ºC	+0.4247	0.4414
Cl^- (0.1%)	+0.8721	0.5702
Cl^- (3%)	+0.5493	0.4636
AcOH (0%)	+0.7016	0.5060
AcOH (3%)	+0.7197	0.5809

4.4 Selection of Stainless-Steel grades

The selection of an appropriate SS grade for food processing equipment is rarely straightforward. In practice, it is largely experienced based rather than data driven, a consequence of the limited availability of systematic corrosion data under realistic food processing conditions and the absence of standardized selection methods for this field.

Conventional metrics such as PREN provide an orientative ranking of pitting resistance based on alloy composition, as discussed in the theoretical section. However, PREN does not account for environmental variables such as chloride concentration, temperature, pH or the presence of organic species, nor for surface preparation effects or microstructural heterogeneity. It is therefore a useful starting point but insufficient for making definitive SS selection decisions in environments as chemically complex as food processing streams. Similarly, the Critical Pitting Temperature (CPT) and Critical Crevice Temperature (CCT) are valuable tools for characterizing the temperature thresholds at which pitting and crevice corrosion initiate, and for distinguishing these from transpassive breakdown. However, these parameters are sensitive to the specific test setup, sample preparation and electrolyte composition, all of which can differ substantially between studies and from real service conditions. Thus, PREN, CPT and CCT are useful comparative indicators within a controlled experimental context rather than as directly transferable design criteria for industrial applications.

More recently, pitting engineering diagrams have been proposed as a practical tool for guiding SS selection based on electrochemical data [3, 77]. These approaches map the experimental E_{pit} values across a range of conditions and define operational safety regions, offering a more condition specific basis for selection than PREN alone. The validity of this approach for the experimental setup used in this project was previously demonstrated for 316L [4, 5], and is extended here to the comparison between DSS 2205 and 254 SMO. Figure 20 provides a complementary three-dimensional visualization of the E_{pit} /E_{break} surfaces for each grade as a function of temperature and chloride concentration, constructed using bilinear interpolation between experimental points, using *surf* function in MATLAB. This surface representation helps identify the regions of the temperature-chloride space where the advantage of 254 SMO over 2205 DSS becomes most and least pronounced.

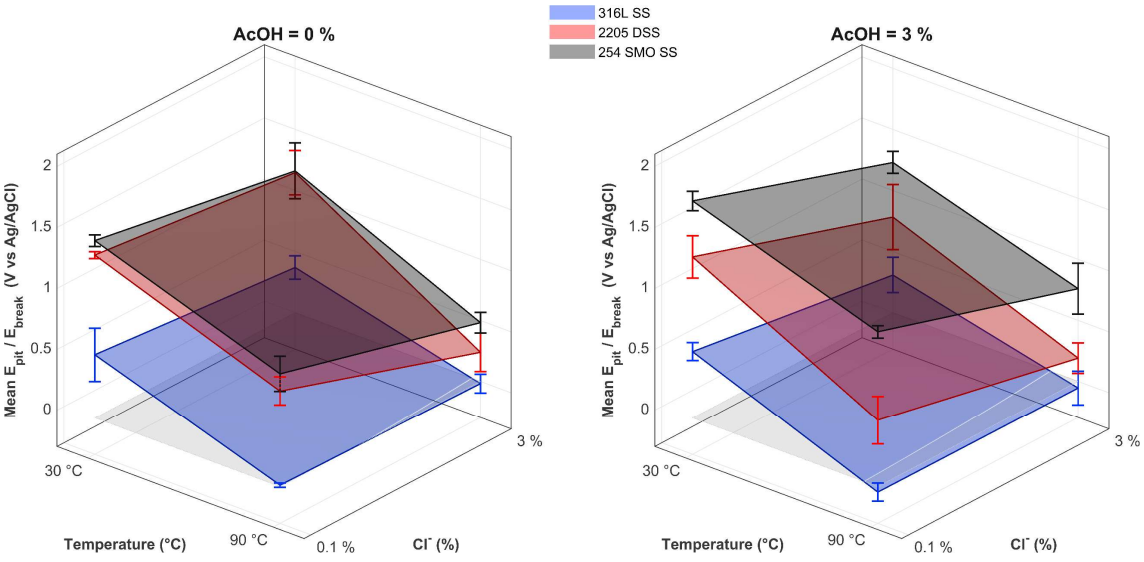

Figure 20: *3D visualization of E_{pit} /E_{break} surfaces for each grade as a function of temperature and chloride concentration with 0% and 3% AcOH. Notably, the distance between 254 SMO and 2205 Duplex increases significantly in presence of AcOH.*

4.4.1 Elimination of 316L SS

Based on the results presented in the previous section and consistent with published recommendations [78], 316L is not considered a viable candidate for the conditions studied in this project. At 0.1% Cl^-, which is already at or beyond the recommended upper limit for 316L in critical food processing applications [78], and particularly at 90°C, the passive oxide layer degrades to the point where E_{pit} falls to near-zero or negative values regardless of the other variables. Under these conditions the material offers essentially no passive margin against pitting corrosion, and the addition of further aggressive factors such as higher chloride or elevated temperature produces negligible additional deterioration simply because the passive film is already saturated. Selecting 316L for components operating under these conditions would introduce an unacceptable risk of corrosion induced failure, with potential consequences for equipment integrity, production continuity and food safety. The following analysis therefore focuses exclusively on 2205 DSSS and 254 SMO as candidates. With 316L eliminated, the practical question is when DSS 2205 is sufficient and when 254 SMO is necessary. Across all conditions, 254 SMO shows a mean E_{pit}/E_{break} approximately 5.5 times that of 316L and 1.4 times that of DSS 2205, while DSS 2205 is approximately 3.8 times higher than 316L. While 254 SMO is clearly superior in terms of pitting resistance, the practical question is whether this advantage is large enough under a given set of conditions to justify its higher cost in terms of raw material, manufacturing complexity and machinability.

4.4.2 Framework for Grade Comparison: E_{pit} /E_{break} Distributions and Safety Limits

To structure the comparison between DSS 2205 and 254 SMO, a safety based evaluation framework was applied using the pitting engineering diagrams shown in Figure 21, using *interp2* function in MATLAB. For each grade and condition, a lower safety limit (denoted as E_{safe}), was defined as the mean E_{pit}/E_{break} minus one standard deviation ($E_{safe} = \mu(E_{pit}/E_{break}) - \sigma$). One interpretation that could be given is that below E_{safe} the probability of pitting initiation under short-term service exposure could be considered low. An upper limit (β), defined as the mean plus one standard deviation ($\beta = \mu(E_{pit}/E_{break}) + \sigma$), indicates the region above which transpassive dissolution or other high-potential processes dominate. Between these two limits lies the region of expected pitting occurrence, whose width reflects the intrinsic stochastic variability of pit initiation in this project. The two chloride concentrations tested (0.1% and 3%) were connected by linear interpolation following the trend established in previous work under the same setup [4, 5], in which E_{pit}/E_{break} decreases with increasing chloride concentration.

4.4.3 SS grade selection based on conditions

For 30°C, 0.1% Cl^-, without AcOH (Figure 21 A), both DSS 2205 and 254 SMO show E_{break} values that fall in the transpassive region, with the characteristic low standard deviations discussed in the previous section. The mean E_{break} values differ by only 0.118 V. Given that both grades show very high resistance and very low

variability, and that the two values are close enough that the practical difference in pitting risk is low, DSS 2205 could be a more cost-effective candidate under these conditions. The small gap in E_{break} and the very low probability of pitting for both grades suggest that the cost for 254 SMO could be difficult to justify here, although other factors should be considered, such as the possibility and cost of machining the different parts of the modules, among others.

For 30°C, 3% Cl^-, without AcOH (Figure 21 A), the mean E_{pit}/E_{break} values of DSS 2205 and 254 SMO differ by only 0.013 V, making them practically indistinguishable in terms of average pitting resistance. Notably, the standard deviation of DSS 2205 is smaller than that of 254 SMO in this condition. Given near identical mean values and slightly lower variability, DSS 2205 tends to be the best appropriate selection, providing effectively equivalent pitting resistance at lower cost, if technical feasibility allows it for a reasonable price.

For 90°C, 0.1% Cl^-, without AcOH (Figure 21 B), the difference between grades widens to 0.143 V, with 254 SMO showing the higher E_{break}. Both values remain at relatively high potentials, suggesting adequate resistance for both grades. However, the greater separation compared to the 30°C conditions and the higher temperature make the choice less clear. DSS 2205 may still represent a viable and cost-effective alternative, but the narrowing safety margin warrants careful consideration. Further data on component lifetime and service costs for both grades under these conditions would be needed to make a more informed selection.

For 90°C, 3% Cl^-, without AcOH (Figure 21 B), which is one of the most aggressive conditions in this study, the clear advantage of 254 SMO makes it the most suitable selection under these conditions. The mean E_{pit}/E_{break} difference between the two grades is 0.243 V, occurring at medium-low potentials where differences in pitting resistance are most consequential. Furthermore, the variability of DSS 2205 is larger than that of 254 SMO under these conditions, meaning that the worst-case pitting event for DSS 2205 falls at substantially lower potentials than for 254 SMO. Under these conditions, it could be said that 254 SMO is the most appropriate selection.

For 30°C, with 3% AcOH (Figure 21 C), The protective effect of AcOH on 254 SMO, established in the previous section, significantly amplifies the advantage of this grade when AcOH is present. At 0.1% Cl^- and 30°C with AcOH, the separation between DSS 2205 and 254 SMO is substantially larger than without AcOH. The E_{break} values of DSS 2205 remain at relatively high potentials, however, and the question of whether the improved resistance of 254 SMO justifies its additional cost remains open. DSS 2205 continues to offer good pitting resistance under these conditions, but the widening gap compared to the no AcOH case and the difference in component lifetime between the two grades should be factored into the decision. At 3% Cl^- with AcOH at 30°C, the large variability of DSS 2205 and the significant separation in mean E_{break} values make 254 SMO to be a more appropriate candidate.

For 90°C, with 3% AcOH (Figure 21 D), one of the most aggressive conditions, 254 SMO is unambiguously the superior candidate. The inhibitory effect of AcOH elevates E_{pit}/E_{break} for 254 SMO while simultaneously reducing it for DSS 2205, producing the largest grade separation observed across all conditions tested. At 3% Cl^- and 90°C with AcOH, 254 SMO shows E_{break} values substantially higher than DSS 2205 due to the ennoblement effect, while DSS 2205 shows both lower values and greater variability. At 0.1% Cl^- under the same temperature and AcOH conditions, DSS 2205 E_{break} is lower than without AcOH, and while it could still theoretically be considered, the data strongly favour 254 SMO under these aggressive combined conditions.

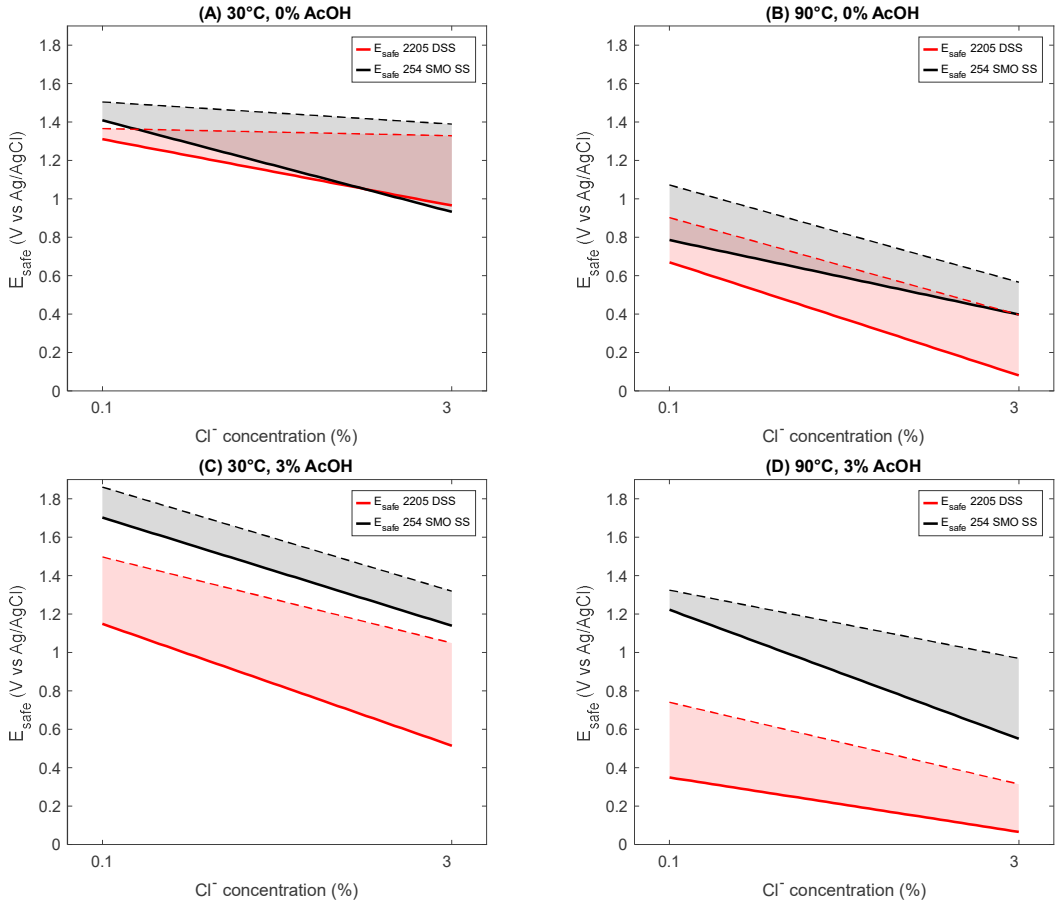

Figure 21: *Pitting engineering diagrams for 2205 DSS and 254 SMO SS. Below the lower limit E_{safe}, the probability of pitting initiation is low. Between limits the regions exhibit high probability of pitting or transpassive dissolution.*

4.4.4 Introduction of SS selection guidelines

The analysis presented here can serve as a practical baseline for guiding SS grade selection in food processing units for Tetra Pak involving the conditions studied. The conclusions are summarized as follows. At mild conditions of 30°C and low chloride, DSS 2205 provides pitting resistance effectively equivalent or sufficient to 254 SMO and represents a more cost-effective choice, if the machinability and weldability allow it for a fair cost. As temperature increases to 90°C and chloride concentration rises to 3%, the advantage of 254 SMO becomes progressively more significant, and at the most aggressive conditions it tends to be the necessary selection. The presence of acetic acid further amplifies this difference due to the grade specific inhibitory effect of AcOH on 254 SMO, making the case for 254 SMO stronger whenever acetic acid is present alongside high chloride and elevated temperature.

It is important to remark that these conclusions are based on pitting potential data obtained under controlled laboratory conditions, and translating them to real service environments requires consideration of additional factors. Some of there, are the suitability of the cleaning process (CIP and SIP) for the selected grade, other processing variables (like for example design pressure and flow regime), the machinability and weldability of each grade for the specific geometries required, the surface finish achievable within the Ra < 0.8 µm food-grade criterion, and the total cost of materials and processing for both Tetra Pak and the end customer. In this section, the concept of a service potential (denoted as $E_{service}$) is proposed, representing the potential at which food processing units operate in practice, which could be introduced as guideline for future development. Since $E_{service}$ is not fixed but fluctuates in reality due to factors such as temperature variations, pressure drops and changes in fluid chemistry within heat exchangers and other process equipment, establishing a safety margin between the distribution of $E_{service}$ values and the stochastic distribution of E_{pit} would provide a more rigorous basis for grade selection. Another factor proposed could be introduced as $E_{\alpha} = E_{corr} + \Delta E$, where ΔE is a safety factor reflecting operational variability, though defining this factor rigorously for the complexity of real food processing streams

remains a significant challenge. Thus, values of $E_{service}$ should be below E_{α} limit to prevent high risk of pitting corrosion.

The variability of E_{pit} also deserves explicit consideration in any future selection methodology. Mean E_{pit} values alone can be misleading, since a grade with a moderately high mean but low variability may provide more reliable protection in service than one with a high mean but large scatter. Particularly in the case of DSS 2205 whose duplex microstructure inherently produces wider pitting potential distributions than single-phase alloys. Future work incorporating Weibull or extreme-value statistical analysis of replicate E_{pit} data could provide a more complete probabilistic basis for grade selection, and the integration of other parameters measured in this project such as repassivation potentials (E_{prot}), which would add a further dimension by capturing the material's ability to arrest pitting once initiated. Together, these directions could move the field towards a more systematic and data-driven approach to SS grade selection for food processing equipment, reducing reliance on experience alone and enabling more informed, condition specific decisions.

4.5 Results for the adaptation of welded 254 SMO SS

After welding the 254 SMO samples, three distinct surface regions were visible: the weld metal (WM) in the center, the heat affected zone (HAZ) on each side, and the base metal (BM) near the outer edges. The position and proportion of each region varied between samples. An example of a welded sample surface exposing each region can be seen in Figure 22.

Before electrochemical testing could begin, a difficulty arose. The welding process caused small radial expansion of the cylindrical sample due to heat, increasing the diameter beyond the nominal 12 mm and not allowing the sample to introduce into the test chamber. This was resolved by manually polishing the cylindrical surface using a lathe in the workshop where the setup is located, so that the sample was secured in the chuck, rotated, and slightly removed metal by hand with a file for under a minute until the diameter was reduced sufficiently to allow adequate insertion of the sample in the test chamber.

When inserting the sample into the test chamber, it was observed that for all samples, the 7 mm internal diameter O-ring was exposing a surface area which was covering primarily the WM and a small portion of the HAZ, with no observable exposure of the BM near the outer edges. This phenomenon varied between samples. This geometry meant that the CPDP measurements were capturing the electrochemical response of the weld metal and, in a smaller extent, the HAZ. Another difficulty was observed at the start and end of the weld line, where the surface was slightly lower than the surrounding area probably due to metal contraction, creating visible gaps between the O-ring and the sample surface. Combined with the height difference between the high WM and the lower HAZ and BM regions, these irregularities produced an uneven seal, introducing the risk of electrolyte leakage and, more critically, of solution becoming trapped between the O-ring and the surface, creating conditions that could promote crevice corrosion. These irregularities can be seen in Figure 25 a).

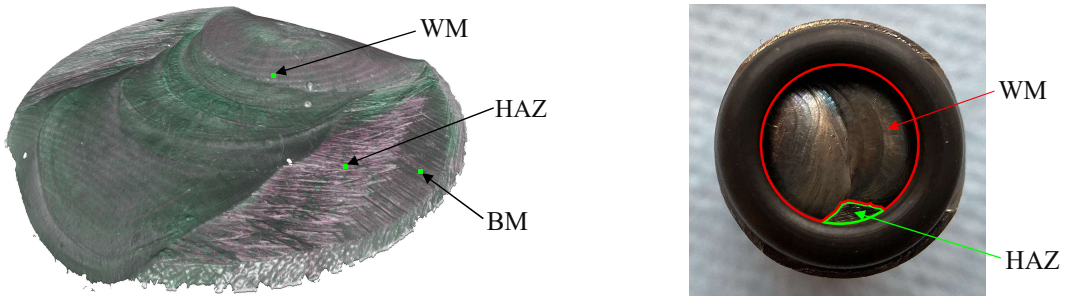

Figure 22: *(a) Example of welded 254 SMO sample surface exposing three different surfaces: welded metal (WM), heat affect zone (HAZ) and base metal (BM). (b) Example of position and proportion of each region exposed before CPDP. In all samples WM was the dominant region with small proportions of HAZ.*

The conditions selected for the experiments were aggressive conditions where 254 SMO is usually selected in practice, such as 90°C without AcOH at two chloride concentrations, 0.1% and 3% Cl^-. The CPDP curves obtained showed a behaviour that was considerably more complex and variable than the previous ones without

welding. In several cases E_{pit} was difficult to identify, since there was a lot of uncertainty. The most interpretable curve, shown in Figure 23, exhibited a significant feature, which was a gradual current increase between approximately 0.16 V and 0.24 V vs Ag/AgCl, followed by a partial stabilization of current between 0.24 V and 0.26 V, before a sharp and sustained current jump at 0.26 V that was identified as E_{pit}. This behaviour was observed in several ways across the other curves as well. Two possible explanations are proposed. The first is that the initial current rise could correspond to a growing but nonstable pit that does not sustain propagation because the product of current and pit depth does not exceed the critical limit for stable growth, causing a partial repassivation and current plateau before a stable pit finally initiates at the sharper E_{pit} event [79]. The second is attributed to two regions response, which could reflect the simultaneous measurement of WM and HAZ regions with different susceptibilities, where WM, being richer in inclusions and microstructural heterogeneities, could begin to pit at lower potentials around 0.16 V, while the less affected region (HAZ) maintains partial passivity and only undergoes breakdown at higher potentials, contributing to the main current jump [80]. Both explanations remain uncertain and would require future work to confirm the phenomenon behind. An additional source of uncertainty is the distance between the reference electrode and the sample surface, where the WM is elevated above the surrounding HAZ and BM, and thus, the effective reference electrode distance may differ from the approximately 4 mm used in all other experiments, potentially introducing measurement differences from what regions are actually being measured.

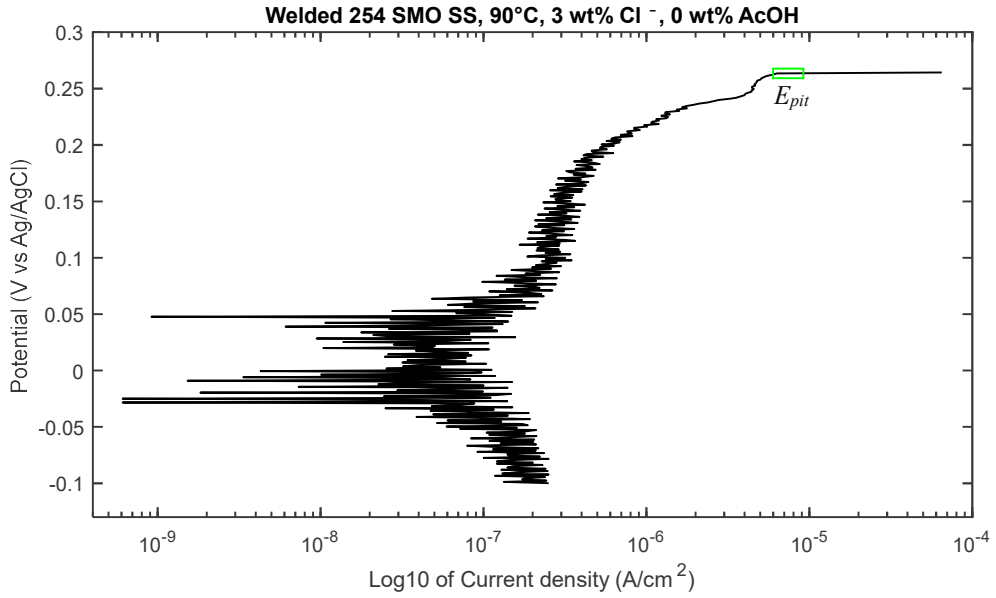

Figure 23: *Example of CPDP curve at 90°C, 3% Cl^- and 0% AcOH, showing E_{pit}. Before E_{pit} a small stabilization region is observed.*

OCP values during the stabilization period showed significant larger fluctuations than the ones observed for the unwelded 316L, DSS 2205 and 254 SMO samples, which could be due to the greater surface heterogeneity of the welded specimens. This suggests that longer stabilization times may be needed for welded samples in future work under these conditions.

The mean E_{pit} values obtained for welded 254 SMO at 90°C are shown in Figure 24 alongside the base metal results for 316L, DSS 2205 and 254 SMO. The welded 254 SMO shows a mean E_{pit} approximately 0.103 V lower when increasing Cl^-. At the same time, mean E_{pit} of welded SMO is lower than the unwelded samples across both chloride concentrations, which is physically reasonable given the microstructural heterogeneity and surface oxide formation in the weld zone. It can be observed that the welded material does not show the same linear beahviour of decrease in E_{pit} with increasing Cl^- concentration that is observed for 2205 Duplex and 254 SMO. However, it is important to mention that a direct comparison between the welded and unwelded results is not reasonable for two reasons. First, the uncertainty about whether the measured E_{pit} values correspond to pitting initiation or to some combination of weld zone effects makes the comparison uncertain. Second, the surface preparation was not consistent, since the unwelded samples were ground with 220 SiC paper and allowed to oxidize for seven days before testing, while the welded samples received no grinding and were tested with the welded surface intact, meaning that the results compared are not equivalent.

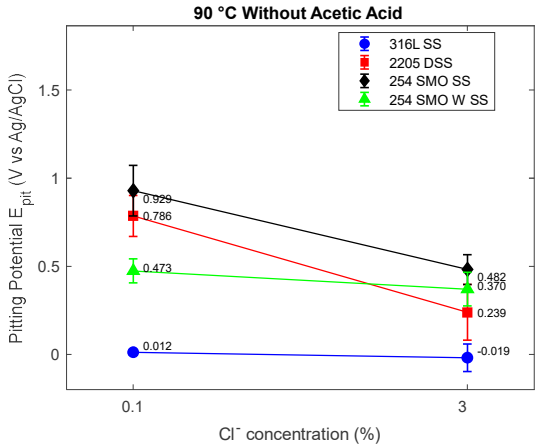

Figure 24: *Mean Epit values for SS base metal grades and the unwelded 254 SMO at 90ºC, (0,1% and 3%) Cl^- without AcOH.*

Despite these limitations, this study showed that CPDP measurements on welded samples are adaptable for the setup and can produce meaningful electrochemical responses, including clear localized corrosion (although E_{pit} was difficult to determine) confirmed by hysteresis in all experiments. These results suggest that with a more carefully sample preparation, considering whether to grind the surface, whether to use shielding gas, type of welding, and the number of regions that are desired to be measured or how to isolate specific weld zones (WM, HAZ or BM) for independent testing, this approach could be developed into a more reliable method for evaluating the corrosion resistance (specifically identify E_{pit} with less uncertainty) of welded components under simulated food processing conditions. Additionally, it should be taken into consideration the level of the different regions on the sample that can create gaps in the interface between the O-ring and sample surface. The question of which zone to measure and how to prepare the surface consistently should be defined before, taking into consideration the industrial application of interest and the fabrication constraints of real food processing equipment components, where the welding approach for different grades can vary and present different difficulties.

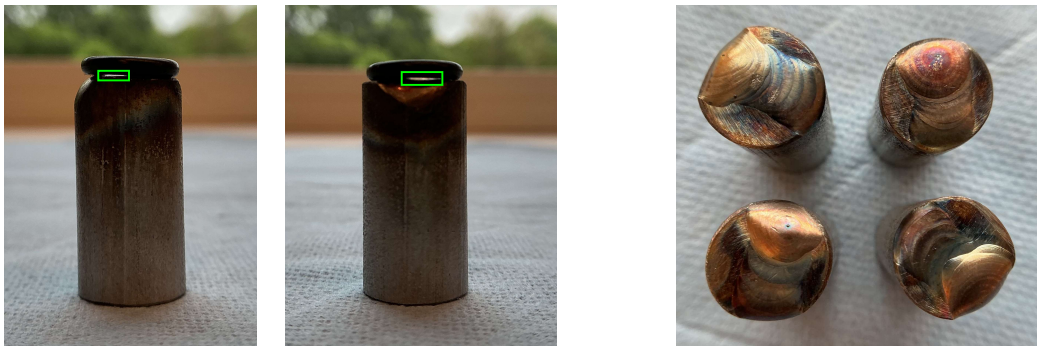

(a) (b)

Figure 25: *(a) Irregularities between the O-ring and sample surface created visible gaps, allowing the possibility of solution leakage. O-ring is unstressed due to not being tight into the test chamber. (b) Different positions and variability of each region (WM, HAZ, BM) for different welded 254 SMO samples.*

5. Conclusions

The project successfully confirmed the introduction of the new SS grades (2205 DSS and 254 SMO) evaluating their pitting corrosion resistance under representative processing conditions in the food industry. The E_{pit}/E_{break} values obtained are consistent with the expected hierarchy based on the PREN values of each grade, such that 254 SMO is the most resistant, followed by 2205 Duplex and then 316L. The frequent occurrence of transpassive dissolution combined with other processes for 2205 DSS and 254 SMO, particularly at high potentials, prevented in many cases the observation of pitting through hysteresis. In these situations, E_{break} can be used as a practical indicator of resistance to localized corrosion for future studies. Between SS grades, temperature was significantly the most limiting factor. The increase from 30°C to 90°C significantly degraded the passive oxide layer, especially in 316L, to the point where additional Cl^- or AcOH had little further effect, due to saturation of the damage already induced by temperature. Chloride concentration was the second most limiting factor, while the effect of acetic acid proved to be the most ambiguous, since it slightly reduced E_{pit}/E_{break} in 316L and 2205 DSS, while for 254 SMO it produced a significant increase in these potentials, suggesting an inhibitory effect whose mechanism remains unclear and deserves further study.

Crevice corrosion emerged in this study as a relevant phenomenon across all SS grades, though with different intensity. It was more noticeable at low Cl^- concentrations and low temperatures, appearing less frequently at higher temperatures. For 316L, it occurred clearly and consistently, while for 2205 DSS and 254 SMO it was less pronounced, with pitting becoming the dominant event. Notably, both higher alloyed grades showed similar susceptibility to crevice corrosion in the polarization curves, suggesting that 2205 DSS already provides sufficient resistance to suppress it, and 254 SMO, despite its higher PREN, behaves comparably under these conditions. Whether the observed current truly represents crevice corrosion or passive region activity remains unclear for these two alloys, and future work should address this alongside improvements to the test chamber design.

The variability observed across SS grades also illustrated practical physical differences that can be further be used for SS grade selection. For 316L, low overall scatter was largely a consequence of the thermal saturation effect at 90°C, which forced all replicates to low potential values around cero, attributed to a degraded passive film. For 2205 DSS, higher variability suggested to be mostly attributed to its duplex microstructure, where the differential surface exposure of ferritic and austenitic phases after grinding could shift the electrochemical response between replicates, making it for the SS grade selection sometimes less reliable and is a phenomenon that would be beneficial to confirm through post CPDP techniques on the surface. For 2205 DSS and in a larger extent in 254 SMO, low standard deviation was observed in some conditions where E_{break} fell in the transpassive region, attributable with a more deterministic behaviour in this region, governed by thermodynamic boundaries in the Pourbaix diagram, compared to the stochastic nature of pitting initiation at inclusions and surface defects. Within this region, E_{break} tended to occur at higher potentials in 254 SMO than in 2205 DSS, which could be explained by differences in the thermodynamic boundaries depending on the chemical composition and microstructure of each alloy. This phenomenon could be beneficial to study it.

Pitting engineering diagrams developed in this work could be use as practical tool for Tetra Pak to help them to select the most appropriate SS grade based on the process conditions of new food products. However, for real-world application, it would be necessary to expand the experimental range to intermediate temperature and Cl^- concentration values, and to translate these data into actual service conditions, taking into account factors such as the cleaning process (CIP/SIP), the weldability and machinability of each grade, the required surface finish ($R_a < 0.8$ µm), and the total production cost, which is of interest to Tetra Pak. Regarding the comparison between grades in pitting engineering diagrams, 316L was eliminated as a viable candidate under the experimental conditions of this project and cannot be recommended for critical food processing applications within these conditions. These diagrams addressed that 2205 DSS and 254 SMO showed very high and comparable pitting resistance at low temperatures, making 2205 Duplex often a suitable cost-effective candidate, while shifting to high temperatures and in the presence of AcOH the gap widens clearly in favour of 254 SMO, which emerges as a better SS grade choice under aggressive conditions.

The adaptation of welded samples confirmed its suitability to CPDP for this setup. However, the greater surface heterogeneity of the weld zone, heat-affected zone and base metal introduced uncertainty as if what was measured was E_{pit}, together with practical challenges including O-ring/surface sample irregularities and the risk of crevice

corrosion at the weld geometry. The results address guidelines for the development of a consistent and well-defined sample preparation protocol, where the decision of the chosen factors should be made based on Tetra Pak's welding practices, which would be beneficial when it comes to assess corrosion and evaluate it with base metal SSs and expand the grade selection.

6. Future Work

- **Post-CPDP surface analysis:** In conditions where the distinction between E_{pit} and E_{break} is ambiguous (and hysteresis might not reveal it clearly), SEM analysis of tested samples could be done and would confirm whether localized corrosion occurred. Also, doing XPS analyses of the passive film could be beneficial, particularly to characterize the Cr(III) to Cr(VI) transformation in the transpassive potential range, which would complement this and help identify the potential range where this phenomenon happens.
- **Transpassive region limits for 2205 DSS and 254 SMO SS:** The observation that the transpassive region occurs at higher potentials in 254 SMO than in DSS 2205 suggests differences in the thermodynamic stability limits of the passive film. Several techniques could be beneficial, such as CALPHAD-based modelling and quantum chemistry simulations using DFT, that could be used to map how alloy composition and microstructure shift the Pourbaix diagram boundaries for each SS grade. Other complementary methods could be beneficial by assessing Cl^- or temperature limits when doing CPDP at which this phenomenon occurs.
- **Pit initiation in 2205 DSS:** the higher variability within the passive region of 2205 Duplex and its dual phase microstructure from the results and literature, raised the question of where pitting initiates. It could be beneficial the use of SEM and EBSD to identify in which phase pitting initiates, which could help to explain the high variability in E_{pit} between replicates and how the fraction of the most exposed surface after grinding could be attributed to a more active or stable response.
- **Crevice corrosion:** Similarly to CCT, defining threshold limits for crevice corrosion in terms of Cl^- concentration and temperature would be beneficial. This would help predict when crevice corrosion is likely to occur for each SS grade under the given setup, particularly for 2205 Duplex and 254 SMO, which tend to suppress it earlier due to their higher PREN. Establishing these boundaries could improve SS grade selection decisions, especially considering that crevice corrosion remains one of the most challenging forms of localized corrosion in the food industry.
- **Inhibitory mechanism of AcOH in 254 SMO:** The presented phenomenon is complex to study and remains to be established. A starting point could be doing ATR-FTIR analysis of the sample surface after testing, which could identify adsorbed acetate species and provide initial evidence for the inhibitory mechanism, although challenges might occur. This should be combined with surface composition analysis before and after exposure to establish whether AcOH modifies the passive film chemistry specifically in 254 SMO.
- **Reverse scan and E_{prot} measurement:** The reverse scan should be completed for all experimental conditions to obtain E_{prot} for DSS 2205 and 254 SMO. This would allow repassivation behaviour to be evaluated systematically and would reduce ambiguity about whether current increases correspond to localized corrosion or transpassive dissolution. Standardizing the potential reversal criterion across all grades within a study would improve comparability. As a practical recommendation, a maximum potential of around 1.0 – 1.2 V vs Ag/AgCl is suggested when only pitting is of interest for higher alloys. If transpassive behaviour is also to be characterized, a small number of preliminary tests should be run first to determine where the transpassive current rise occurs for each grade under the least aggressive conditions, allowing the reversal potential limit to be set accordingly for the rest of experiments.
- **OCP stabilization:** increase the open circuit potential measurement time (especially for welded samples without shielding gas, where OCP was still fluctuating significantly at 30 minutes) to start CPDP tests from a more stable state and obtain more reliable parameters.
- **Exploration of intermediate values:** study Cl^- concentrations between 0.1% and 3% and intermediate temperatures between 30°C and 90°C to confirm the linearity of E_{pit} /E_{break} behaviour and improve the reliability of the pitting engineering diagrams. This is especially important for determining the conditions under which DSS 2205 remains a feasible candidate to 254 SMO.
- **Test chamber redesign:** redesign the test chamber to eliminate the crevice corrosion phenomenon observed, while also controlling the screw pressure on the O-ring to ensure consistency (same surface density exposed to CPDP) between experiments.
- **Method for welded samples:** Future work for testing welded specimens should take into account when planning the experiments: (1) Which regions to measure (WM, HAZ, BM). (2) Whether to measure regions separately or combined. (3) The shielding gas and type of welding. (4) Whether to grind before or/and after welding, which should reflect close Tetra Pak welding conditions when manufacturing. (5) Consistent positioning and controlled exposed area of each weld region within the O-ring area. (6) Reduce irregularities

produce by height differences between WM and HAZ/BM surface to minimize crevice corrosion risk. (7) It could be considered a test chamber redesign to reduce solution leakage and improve O-ring/surface sample contact. The screw tightening pressure on the O-ring should also be standardized across experiments, as it could influence the exposed surface area and therefore the current density.

- **Validation with real food solutions:** use real food solutions, such as ketchup for example, with conditions similar to those tested to validate the obtained data
- **Development of the Eservice parameter:** formally define the concept of service potential ($E_{service}$) with its safety factor ($E_{\alpha} = E_{corr} + \Delta E$), considering real operating variables such as flow rate, pressure, viscosity, and temperature in the processing equipment. Include estimates of the service lifetime of the selected grade. This last concept presents several challenges.
- **Coated steels:** explore the CPDP behaviour of coated steels and compare it to that of base stainless-steel grades, including comparisons between welded and non-welded samples.

7. Reference

[1] A. Zaffora, F. Di Franco, and M. Santamaria, “Corrosion of stainless steel in food and pharmaceutical industry,” *Current Opinion in Electrochemistry*, vol. 29, p. 100760, Oct. 2021, doi: https://doi.org/10.1016/j.coelec.2021.100760.

[2] A. N. Murray, “Food Safety Assurance Systems: Hygienic Design of Equipment,” *Elsevier eBooks*, vol. 4, pp. 181–188, Jan. 2014, doi: https://doi.org/10.1016/b978-0-12-378612-8.00353-x.

[3] S. H. Mameng, R. Pettersson, and J. Y. Jonson, “Limiting conditions for pitting corrosion of stainless steel EN 1.4404 (316L) in terms of temperature, potential and chloride concentration,” *Materials and Corrosion*, vol. 68, no. 3, pp. 272–283, Jul. 2016, doi: https://doi.org/10.1002/maco.201609061.

[4] F. Waldur, “Effekter av livsmedelsförädling för lokalkorrosion på rostfritt stål 316L,” *Lub.lu.se*, 2022. https://lup.lub.lu.se/student-papers/search/publication/9106769 (accessed May 26, 2026).

[5] E. Håkansson, “Inhibition of Pitting Corrosion in 316L Stainless steel: an evaluation of the phenomena and method to facilitate material selection for processing equipment,” *Lub.lu.se*, 2024. https://lup.lub.lu.se/student-papers/search/publication/9158081 (accessed May 26, 2026).

[6] C. Verma, V. Srivastava, T. W. Quadri, Chaudhery Mustansar Hussain, and E. E. Ebenso, *Smart Anticorrosive Materials*. Elsevier, 2023.

[7] K. D. Mekonnen, “Corrosion fundamentals: Thermodynamics, rate, passivity, types, and control mechanism,” *Results in Surfaces and Interfaces*, vol. 22, p. 100720, Jan. 2026, doi: https://doi.org/10.1016/j.rsurfi.2026.100720.

[8] A. Vidiš, Gábor Laurenczy, Ernst Küsters, Gottfried Sedelmeier, and P. J. Dyson, “High-pressure effects on the Diels–Alder reaction in room temperature ionic liquids,” *Journal of Physical Organic Chemistry*, vol. 20, no. 2, pp. 109–114, Jan. 2007, doi: https://doi.org/10.1002/poc.1131.

[9] M Niinomi, *Metals for biomedical devices.* Cambridge: Woodhead Pub, 2010.

[10] P. Marcus, *Corrosion mechanisms in theory and practice*. Boca Raton: Crc Press, 2017.

[11] X. Zhang, N. Noël-Hermes, G. Ferrari, and M. Hoogeland, “Localized Corrosion of Mooring Chain Steel in Seawater,” *Corrosion and Materials Degradation*, vol. 3, no. 1, pp. 53–74, Feb. 2022, doi: https://doi.org/10.3390/cmd3010004.

[12] P. Pedeferri, *Corrosion Science and Engineering*. Cham: Springer International Publishing, 2018. doi: https://doi.org/10.1007/978-3-319-97625-9.

[13] O. Agboola *et al.*, “A Review on Corrosion in Concrete Structure: Inhibiting Admixtures and Their Compatibility in Concrete,” *Journal of Bio- and Tribo-Corrosion*, vol. 8, no. 1, Dec. 2021, doi: https://doi.org/10.1007/s40735-021-00624-2.

[14] U. Angst , “Chloride induced reinforcement corrosion in concrete,” Jan. 2011. https://nva.sikt.no/registration/0198e7771a21-1d4b8a43-7673-466d-be9e-9442acbb235c

[15] N. Corlett *et al.*, “2.03Crevice Corrosion,” in *Shreir’s Corrosion*, Oxford: Elsevier, 2010, pp. 753–771. doi: https://doi.org/10.1016/B9780444527875.000299.

[16] S.-H. Choi, Y.-R. Yoo, Y.-C. Kim, and Y.-S. Kim, “Effect of Cr, Mo, and W Contents on the Semiconductive Properties of Passive Film of Ferritic Stainless Steels,” *Crystals*, vol. 15, no. 8, p. 723, Aug. 2025, doi: https://doi.org/10.3390/cryst15080723.

[17] Q. Fu, S. Li, D. Niu, and Y. Miao, “Passivation and depassivation of chromium alloy steel bars in concrete: A review,” *Chemical Engineering Journal*, vol. 511, p. 162032, May 2025, doi: https://doi.org/10.1016/j.cej.2025.162032.

[18] Y. Tang and R. Ballarini, “A theoretical analysis of the breakdown of electrostrictive oxide film on metal,” *Journal of the Mechanics and Physics of Solids*, vol. 59, no. 2, pp. 178–193, Nov. 2010, doi: https://doi.org/10.1016/j.jmps.2010.11.002.

[19] Yu. I. Kuznetsov, “Adsorptive Passivation of Iron by Organic Acid Anions,” *Russian Journal of Electrochemistry*, vol. 40, no. 12, pp. 1287–1291, Dec. 2004, doi: https://doi.org/10.1007/s11175-005-0006-2.

[20] Y.-T. Sun, X. Tan, L.-L. Lei, J. Li, and Y.-M. Jiang, “Revisiting the effect of molybdenum on pitting resistance of stainless steels,” *Tungsten*, vol. 3, no. 3, pp. 329–337, Jun. 2021, doi: https://doi.org/10.1007/s42864-021-00099-1.

[21] I. Juraga, I. Stojanović, and B. Ljubenkov, “EXPERIMENTAL RESEARCH OF THE DUPLEX STAINLESS STEEL WELDS IN SHIPBUILDING,” *Brodogradnja : An International Journal of Naval Architecture and Ocean Engineering for Research and Development*, vol. 65, no. 2, pp. 73–85, Jun. 2014, Accessed: May 26, 2026. [Online]. Available: https://hrcak.srce.hr/123484

[22] G. Ran *et al.*, “Comparative statistical analysis of pitting in Two 2205 duplex stainless steel variants,” *npj Materials Degradation*, vol. 8, no. 1, Mar. 2024, doi: https://doi.org/10.1038/s41529-024-00448-8.

[23] Suprapto, T. Sujitno, D. Slamet Pudjorahardjo, H. Suprihatin, I. Zulhendri, and Saefurrochman, “Thin film deposition of tungsten nitride on SS 316 L surface using DC-Sputtering technique,” *Journal of Physics: Conference Series*, vol. 2498, no. 1, p. 012019, May 2023, doi: https://doi.org/10.1088/1742-6596/2498/1/012019.

[24] A. Nouri and C. Wen, “Stainless steels in orthopedics,” *Structural Biomaterials*, vol. 3, pp. 67–101, Jan. 2021, doi: https://doi.org/10.1016/b978-0-12-818831-6.00008-2.

[25] Drápala Jaromír, “Influence of heat treatment on microstructure and mechanical properties of SUS 316L alloy,” *Confer.cz*, Oct. 24, 2018. https://www.confer.cz/metal/2018/1305-influence-of-heat-treatment-on-microstructure-and-mechanical-properties-of-sus-316l-alloy (accessed May 26, 2026).

[26] V. Durga, T. Buddi, P. Rahul Kanth, and Kosaraju Satyanarayana, “Microstructural and corrosion resistance study on plasma arc welded joints of AISI 304 and AISI 316,” *Advances in Materials and Processing Technologies*, vol. 6, no. 2, pp. 189–205, Feb. 2020, doi: https://doi.org/10.1080/2374068x.2020.1732158.

[27] H. Lihua, W. Lu, J. Jie, W. Zhu, Z. Guohui, and Z. Lei, “Study on Corrosion Resistance of 316L and 2205 Stainless Steels in High CO2 Environment,” *ResearchGate*, vol. 55, no. 9, Sep. 2022, doi: https://doi.org/10.16577/j.issn.1001-1560.2022.0246.

[28] W. Lv, C. Pan, W. Su, Z. Wang, S. Liu, and C. Wang, “Atmospheric corrosion mechanism of 316 stainless steel in simulated marine atmosphere,” *Corrosion Engineering Science and Technology The International Journal of Corrosion Processes and Corrosion Control*, vol. 51, no. 3, pp. 155–162, Jul. 2015, doi: https://doi.org/10.1179/1743278215y.0000000042.

[29] A. Higelin, S. Le Manchet, G. Passot, S. Cissé, and J. Grocki, “Heat-affected zone ferrite content control of a duplex stainless steel grade to enhance weldability,” *Welding in the World*, vol. 66, no. 8, pp. 1503–1519, Jun. 2022, doi: https://doi.org/10.1007/s40194-022-01326-0.

[30] J. C. M. Farrar, “The Alloy Tree: A Guide to Low-alloy Steels, Stainless Steels and Nickel-base Alloys 1855737663, 9781855737662, 9781855739925 - EBIN.PUB,” *ebin.pub*, 2019. https://ebin.pub/the-alloy-tree-a-guide-to-low-alloy-steels-stainless-steels-and-nickel-base-alloys-1855737663-9781855737662-9781855739925.html#A+Farrar (accessed May 26, 2026).

[31] S. R. F. Batista and S. E. Kuri, “Aspects of selective and pitting corrosion in cast duplex stainless steels,” *Anti-Corrosion Methods and Materials*, vol. 51, pp. 205–208, Jun. 2004, doi: https://doi.org/10.1108/00035590410533156.

[32] H. Zeng, Y. Yang, L. Liu, and M. Li, “Pitting and crevice corrosion evolution characteristics of 2205 duplex stainless steel in hot concentrated seawater,” *Journal of Solid State Electrochemistry*, vol. 25, no. 5, pp. 1555–1565, Mar. 2021, doi: https://doi.org/10.1007/s10008-021-04935-9.

[33] D. Gupta, A. Bansal, and S. Jindal, “Duplex Stainless Steel-2205; A short review of alloy addition and welding behavior,” *International Journal of Current Engineering and Technology*, vol. 14, pp. 113–119, 2024, Accessed: May 26, 2026. [Online]. Available: https://ijcet.evegenis.org/index.php/ijcet/article/view/1280

[34] V. Yakubov, M. Lin, A. A. Volinsky, L. Qiao, and L. Guo, “The hydrogen-induced pitting corrosion mechanism in duplex stainless steel studied by current-sensing atomic force microscopy,” *npj Materials Degradation*, vol. 2, no. 1, Dec. 2018, doi: https://doi.org/10.1038/s41529-018-0062-1.

[35] A. Vinoth Jebaraj, L. Ajaykumar, C. R. Deepak, and K. V. V. Aditya, “Weldability, machinability and surfacing of commercial duplex stainless steel AISI2205 for marine applications – A recent review,” *Journal of Advanced Research*, vol. 8, no. 3, pp. 183–199, May 2017, doi: https://doi.org/10.1016/j.jare.2017.01.002.

[36] L. de Micheli, C. A. Barbosa, A. H. P. Andrade, and S. M. L. Agostinho, “Electrochemical behaviour of 254SMO stainless steel in comparison with 316L stainless steel and Hastelloy C276 in HCl media,” *British Corrosion Journal*, vol. 35, no. 4, pp. 297–300, Apr. 2000, doi: https://doi.org/10.1179/000705900101501371.

[37] E. A. Abd El Meguid and A. A. Abd El Latif, “Critical pitting temperature for Type 254 SMO stainless steel in chloride solutions,” *Corrosion Science*, vol. 49, no. 2, pp. 263–275, Feb. 2007, doi: https://doi.org/10.1016/j.corsci.2006.06.011.

[38] J. Li, W. Liang, M. Wu, S. Zhang, and W. Zhang, “Microstructure Evolution in the Segregation Area of S31254 Stainless Steel Plate,” *Materials Today: Proceedings*, vol. 2, pp. S319–S324, 2015, doi: https://doi.org/10.1016/j.matpr.2015.05.045.

[39] S. Kou, “Welding Metallurgy,” Oct. 2002, doi: https://doi.org/10.1002/0471434027.

[40] R. P, A. M, A. N, S. A, and P. Prabhakar, “Investigations on induced residual stresses, mechanical and metallurgical properties of CO2 laser beam and pulse current gas tungsten arc welded SMO 254,” *Journal of Manufacturing Processes*, vol. 44, pp. 81–90, 2019, doi: https://doi.org/10.1016/j.jmapro.2019.05.044.

[41] P. J. R. Kumar and A. Baskaran, “Impact of CC and PCTIG Welding on SMO 254 Joints Using Alloy 625 Filler,” *Indian Journal Of Science And Technology*, vol. 17, no. 34, pp. 3553–3566, Sep. 2024, doi: https://doi.org/10.17485/ijst/v17i34.2163.

[42] J. McNicol, B. Narayanan, N. Sridhar, and C. Fink, “Corrosion resistance of austenitic stainless steel welds with no-backing gas,” *Welding in the World*, vol. 67, no. 3, pp. 819–830, Dec. 2022, doi: https://doi.org/10.1007/s40194-022-01442-x.

[43] Jerzy Łabanowski and M. Głowacka, “Heat tint colours on stainless steel and welded joints,” *Welding International*, vol. 25, no. 7, pp. 509–512, Jun. 2011, doi: https://doi.org/10.1080/09507116.2010.540837.

[44] X. Zhao, C. Cheng, T. Cao, J. Zhao, X. Sun, and D. Zhang, “The effect of oxide scale on the corrosion resistance of SUS301L stainless steel welding joints,” *Materials Characterization*, vol. 217, p. 114431, 2024, doi: https://doi.org/10.1016/j.matchar.2024.114431.

[45] L. G. Bland, J. M. Fitz-Gerald, and J. R. Scully, “Metallurgical and Electrochemical Characterization of the Corrosion of AZ31B-H24 Tungsten Inert Gas Weld: Isolated Weld Zones,” *CORROSION*, vol. 72, no. 9, pp. 1116–1132, Sep. 2016, doi: https://doi.org/10.5006/2052.

[46] S. Wang, M. Nishimoto, and I. Muto, “Grinding-induced degradation in the pitting corrosion resistance of stainless steel: insights into passive film and MnS,” *npj Materials Degradation*, vol. 10, no. 1, Feb. 2026, doi: https://doi.org/10.1038/s41529-026-00750-7.

[47] Evert D.D. During, *CORROSION ATLAS : a collection of illustrated case histories.* Joe Hayton, 2018.

[48] A. Taher, “Evaluating corrosion and passivation by electrochemical techniques,” 2016. Available: https://api.semanticscholar.org/CorpusID:54659099

[49] O. M. Ama and S. S. Ray, *Nanostructured Metal-Oxide Electrode Materials for Water Purification*. Springer Nature, 2020. doi: https://doi.org/10.1007/978-3-030-43346-8.

[50] N. Leslie, J. Mauzeroll, K. Wandelt, and G. Bussetti, “Spatially resolved electrochemical measurements,” in *Encyclopedia of SolidLiquid Interfaces (First Edition)*, Oxford: Elsevier, 2024, pp. 461–478. doi: https://doi.org/10.1016/B9780323856690.000040.

[51] R. Ghamsarizade, B. Ramezanzadeh, M. H. Eivaz, J. Aslam, C. Verma, and M. Hussain, “Chapter 12Corrosion measurements in coatings and paintings,” in *Electrochemical and Analytical Techniques for Sustainable Corrosion Monitoring*, Elsevier, 2023, pp. 217–264. doi: https://doi.org/10.1016/B9780443157837.000086.

[52] V. K. Gattu, J. Obregon, W. L. Ebert, and J. E. Indacochea, “Effects of open circuit immersion and vertex potential on potentiodynamic polarization scans of metallic biomaterials,” *npj Materials Degradation*, vol. 8, no. 1, Feb. 2024, doi: https://doi.org/10.1038/s41529-023-00420-y.

[53] C. Prakash, Z. Sun, Y. Zeng, N. Maeda, and J. Liu, “Electrochemical corrosion measurements in lowconductivity biooils: Decoupling interfacial film memory from bulk electrolyte aging,” *Electrochimica Acta*, vol. 559, p. 148628, 2026, doi: https://doi.org/10.1016/j.electacta.2026.148628.

[54] E. M. Sherif, Almajid, Abdulhakim A, K. A. Khalil, H. Junaedi, and F. H. Latief, “Electrochemical Studies on the Corrosion Behavior of API X65 Pipeline Steel in Chloride Solutions,” *International Journal of Electrochemical Science*, vol. 8, no. 7, pp. 9360–9370, 2013, doi: https://doi.org/10.1016/S14523981(23)129750.

[55] M. M. Goldin *et al.*, “Redox Potential Measurement in Aqueous Solutions and Biological Media,” *ECS Transactions*, vol. 11, no. 21, p. 39, 2008, doi: https://doi.org/10.1149/1.2928905.

[56] S. Esmailzadeh, M. Aliofkhazraei, and H. Sarlak, “Interpretation of Cyclic Potentiodynamic Polarization Test Results for Study of Corrosion Behavior of Metals: A Review,” *Protection of Metals and Physical Chemistry of Surfaces*, vol. 54, no. 5, pp. 976–989, Sep. 2018, doi: https://doi.org/10.1134/s207020511805026x.

[57] Z. Yang *et al.*, “Evolution and corrosion resistance of passive film with polarization potential on Ti5Al5Mo5V1Fe1Cr alloy in simulated marine environments,” *Corrosion Science*, vol. 221, p. 111334, 2023, doi: https://doi.org/10.1016/j.corsci.2023.111334.

[58] A. A., D. G Nair, K. Hansdah, B. Dhal, K. D. Mehta, and B. D. Pandey, “Bioremoval of Chromium (III) from Model Tanning Effluent by Novel Microbial Isolate,” *International Journal of Metallurgical Engineering*, vol. 1, no. 2, pp. 12–16, Aug. 2012, doi: https://doi.org/10.5923/j.ijmee.20120102.01.

[59] J. Milledge, “The cleanability of stainless steel used as a food contact surface: An updated short review,” *Food Science and Technology*, vol. 24, pp. 27–28, Dec. 2010.

[60] A. AlHazaa and N. Haneklaus, “Diffusion Bonding and Transient Liquid Phase (TLP) Bonding of Type 304 and 316 Austenitic Stainless Steel—A Review of Similar and Dissimilar Material Joints,” *Metals*, vol. 10, no. 5, p. 613, 2020, doi: https://doi.org/10.3390/met10050613.

[61] Arthur, T. Ferreira, C. Bolfarini, and G. Y. Koga, “Air carbon arc gouging and submergedarc welding: Insights into sensitization and mechanical behavior of AISI 2205 duplex stainless steel,” *Journal of Materials Research and Technology*, vol. 36, pp. 6196–6218, 2025, doi: https://doi.org/10.1016/j.jmrt.2025.04.273.

[62] A. Malandruccolo, C. Menapace, and I. Giroletti, “Metallurgy, Properties and Applications of Superaustenitic Stainless Steels—SASSs,” *Materials*, vol. 18, no. 13, p. 3079, 2025, doi: https://doi.org/10.3390/ma18133079.

[63] Y. Wu, Y. Du, X. Zhang, Y. Ren, and X. Duan, “Influence of temperature on the corrosion behavior and passive film performance of 2205 DSS in LTMED for treating mine water,” *Electrochimica Acta*, vol. 507, p. 145200, 2024, doi: https://doi.org/10.1016/j.electacta.2024.145200.

[64] H. Zhong *et al.*, “Investigating the influence of Cl^- concentration on galvanic corrosion of stainless steel using wire beam electrode technique,” *Ionics*, vol. 31, no. 11, pp. 12461–12476, 2025, doi: https://doi.org/10.1007/s11581025067397.

[65] A. El and A. El, “Electrochemical and SEM study on Type 254 SMO stainless steel in chloride solutions,” *Corrosion Science*, vol. 46, no. 10, pp. 2431–2444, 2004, doi: https://doi.org/10.1016/j.corsci.2004.01.022.

[66] B. Cai *et al.*, “Susceptibility of 316L stainless steel to crevice corrosion in submersible solenoid valve,” *Materials and Corrosion*, vol. 62, Aug. 2011, doi: https://doi.org/10.1002/maco.201005917.

[67] M. Långberg *et al.*, “Redefining passivity breakdown of super duplex stainless steel by electrochemical operando synchrotron near surface Xray analyses,” *npj Materials Degradation*, vol. 3, no. 1, p. 22, 2019, doi: https://doi.org/10.1038/s4152901900843.

[68] N. J. Laycock and R. C. Newman, “Temperature dependence of pitting potentials for austenitic stainless steels above their critical pitting temperature,” *Corrosion Science*, vol. 40, no. 6, pp. 887–902, 1998, doi: https://doi.org/10.1016/S0010938X(98)000201.

[69] Q. Wang, Q. Wang, X. Wang, F. Liu, and K. Yang, “Untypical Electrochemical Corrosion Behavior of HighNitrogen Austenitic Stainless Steel: NonPitting in Transpassivation,” *Acta Metallurgica Sinica (English Letters)*, vol. 37, no. 10, pp. 1785–1792, 2024, doi: https://doi.org/10.1007/s40195024017438.

[70] C. Man, C. Dong, Z. Cui, K. Xiao, Q. Yu, and X. Li, “A comparative study of primary and secondary passive films formed on AM355 stainless steel in 0.1M NaOH,” *Applied Surface Science*, vol. 427, pp. 763–773, 2018, doi: https://doi.org/10.1016/j.apsusc.2017.08.151.

[71] B. Li, Y. Lang, H. Chen, H. Feng, and Z. Gao, “Exploration of microstructural evolution and corrosion behavior of 254 SMO superaustenitic stainless steel bipolar plates following highspeed tensile deformation,” *Journal of Materials Research and Technology*, vol. 39, pp. 6177–6190, 2025, doi: https://doi.org/10.1016/j.jmrt.2025.11.008.

[72] L. Chen *et al.*, “Insight into electrochemical passivation behavior and surface chemistry of 2205 duplex stainless steel: effect of tensile elastic stress,” *Corrosion Science*, vol. 193, p. 109903, 2021, doi: https://doi.org/10.1016/j.corsci.2021.109903.

[73] C. Yang, Z. Wang, Z. Liu, J. Wang, and L. Zhang, “Effect of hydrogen on passive film and corrosion behavior of 2507 super duplex stainless steel in H2S environment,” *International Journal of Hydrogen Energy*, vol. 171, p. 151254, 2025, doi: https://doi.org/10.1016/j.ijhydene.2025.151254.

[74] C. Park, H. Kwon, and M. M. Lohrengel, “Microelectrochemical polarization study on 25% Cr duplex stainless steel,” *Materials Science and Engineering: A*, vol. 372, no. 1, pp. 180–185, 2004, doi: https://doi.org/10.1016/j.msea.2003.12.013.

[75] B. Zhang *et al.*, “Unmasking chloride attack on the passive film of metals,” *Nature Communications*, vol. 9, no. 1, p. 2559, 2018, doi: https://doi.org/10.1038/s4146701804942x.

[76] N. Sato, “CHAPTER 11MIXED ELECTRODES,” in *Electrochemistry at Metal and Semiconductor Electrodes*, Amsterdam: Elsevier Science, 1998, pp. 373–389. doi: https://doi.org/10.1016/B9780444828064/500118.

[77] Hägg Mameng, Sukanya, L. Wegrelius, and S. Hosseinpour, “Stainless steel selection tool for water application: pitting engineering diagrams,” *Frontiers in Materials*, vol. Volume 11 - 2024, 2024, doi: https://doi.org/10.3389/fmats.2024.1353907.

[78] “Guidelines for Nickel Stainless Steels for Marine Environments, Natural Waters, and Brines (11003),” *Nickelinstitute.org*, 1987. https://nickelinstitute.org/en/resources/technical-guides/guidelines-for-nickel-stainless-steels-for-marine-environments-natural-waters-and-brines-11003/ (accessed May 26, 2026).

[79] P. C. Pistorius and G. T. Burstein, “Growth of corrosion pits on stainless steel in chloride solution containing dilute sulphate,” *Corrosion Science*, vol. 33, no. 12, pp. 1885–1897, 1992, doi: https://doi.org/10.1016/0010938X(92)901915.

[80] J. He, S. Xu, W. Ti, Y. Han, J. Mei, and X. Wang, “The Pitting Corrosion Behavior of the Austenitic Stainless Steel 308L316L Welded Joint,” *Metals*, vol. 10, no. 9, p. 1258, 2020, doi: https://doi.org/10.3390/met10091258.

A Appendix

A.1 Optical surface roughness (R_a) for base metal and welded 254 SMO SS

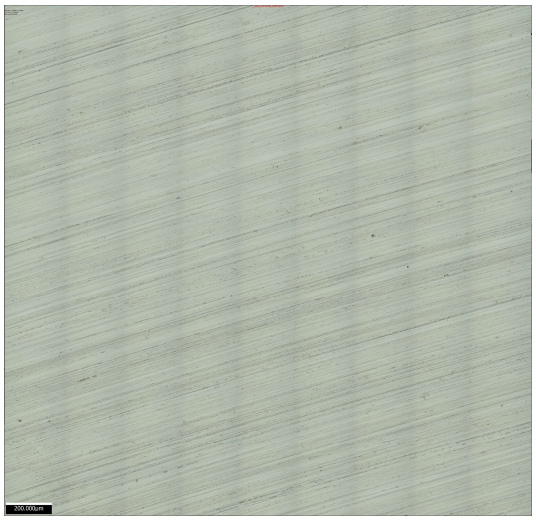

(a)

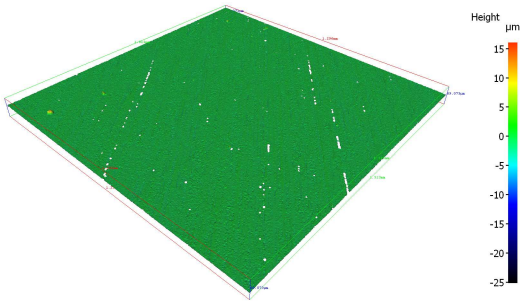

(b)

Histogram Settings

Min. Value:	-2.052	µm
Max. Value:	0.808	µm
Class Width:	0.020	µm

Reset

Statistics

Name	Value	Unit	Description
Elements	13108		Number of data values
Classes	143		Number of histogram classes
Mean Value	-0.099	µm	Mean value of data values
Standard Deviation	0.412	µm	Mean Value of standard deviation

Parameters

Name	Value	Unit	Description
Ra	0.285	µm	Average roughness of profile
Rq	0.424	µm	Root-Mean-Square roughness of profile
Rt	2.849	µm	Maximum peak to valley height of roughness profile
Rz	1.794	µm	Mean peak to valley height of roughness profile
Rmax	2.628	µm	Maximum peak to valley height of roughness profile within a sampling length
Rp	0.797	µm	Maximum peak height of roughness profile
Rv	2.052	µm	Maximum valley height of roughness profile
Rc	1.001	µm	Mean height of profile irregularities of roughness profile
Rsm	66.047	µm	Mean spacing of profile irregularities of roughness profile
Rsk	-2.160		Skewness of roughness profile
Rku	7.866		Kurtosis of roughness profile
Rdq	0.081		Root-Mean-Square slope of roughness profile
Rt/Rz	1.588		Extreme Scratch/Peak value of roughness profile, (>=1), higher values represent larger scratches/peaks
l	4.400	mm	Profile Length
Lc	800.000	µm	LambdaC: cut off wavelength

This page implements the following standard(s): ISO 4287; ASME B46.1-2002 (Refer to the help for more information)

(c)

Figure 26: *Example of a base SS sample under Alicona optical microscope at a 50x magnification. (a) Surface topography. (b) 3D height map visualization. (c) Surface roughness (R_a) parameters according to ISO 4287.*

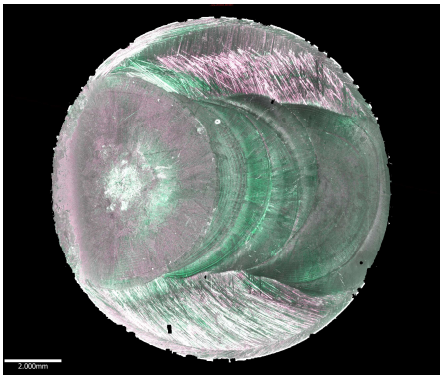

(a)

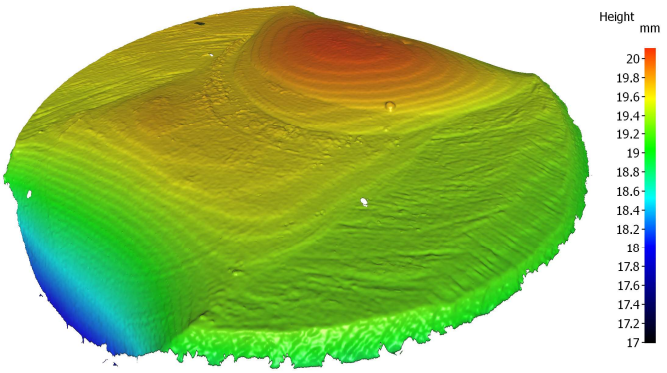

(b)

Figure 27: *Example of a welded 254 SMO SS sample under Alicona optical microscope at a 1.5x magnification. (a) Surface topography. (b) 3D height map visualization, where highest and lowest values correspond to the beginning and end of the welding line (WD). The surface with the lowest height variability was BM, followed by HAZ.*

A.2 Summary of recorded OCP values

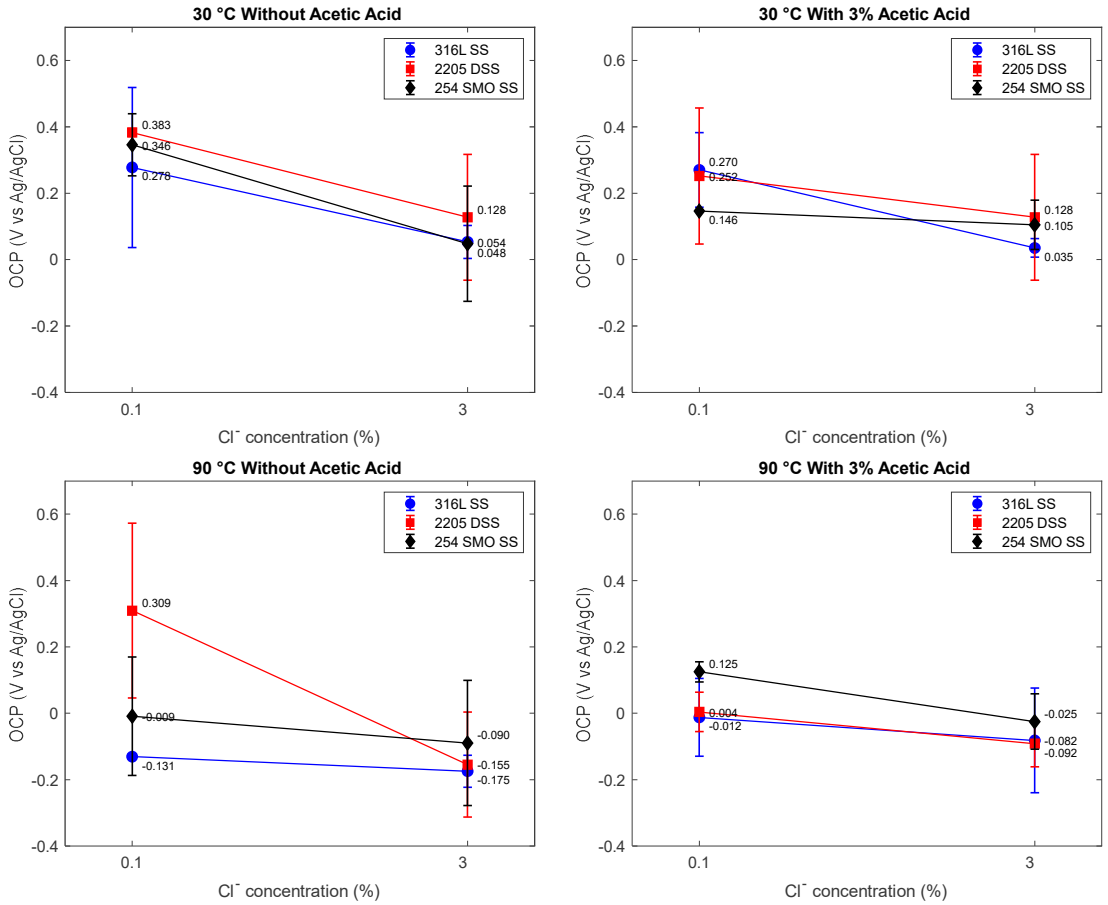

Figure 28: *Summary of mean OCP values for base 316L SS, 2205 DSS and 254 SMO SS.*

A.3 Statistical Data for OCP-E_{corr} discrepancy

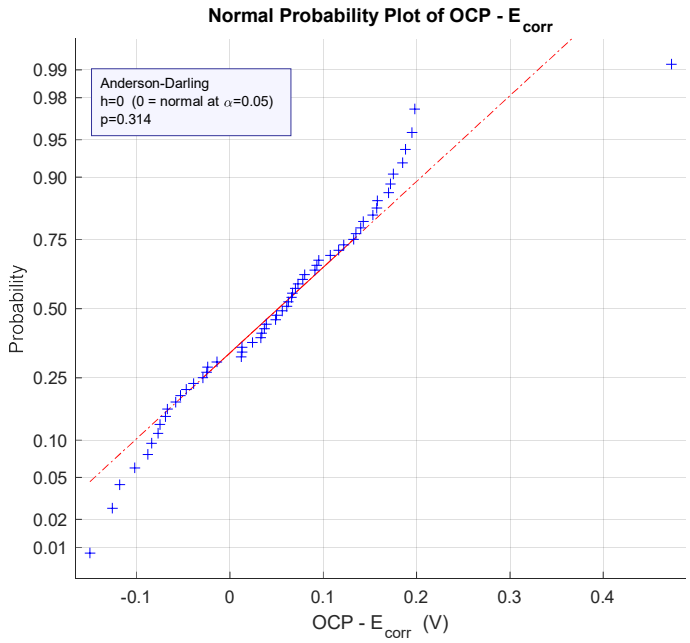

Figure 29: *Anderson-Darling test confirmed normality at α=0.05 allowing the use of parametric ANOVA models. p-value for OCP-E_{corr} was 0.3164, which indicates that data follows a normal distribution and h = 0 indicates that null hypothesis cannot be rejected.*

Analysis of Variance

Source	Sum Sq.	d.f.	Mean Sq.	F	Prob>F
Grade	0.00443	2	0.00222	0.19	0.8305
Temp	0.00404	1	0.00404	0.34	0.5626
Cl-	0.04103	1	0.04103	3.45	0.0689
AcOH	0.00528	1	0.00528	0.44	0.5079
Error	0.61822	52	0.01189		
Total	0.67563	57			

Constrained (Type III) sums of squares.

Figure 30: *ANOVA 1 model results for single factors: Grade, Temp, Cl^- and AcOH. p-values are higher than 0.05, indicating that none of the single factors explains the deviation of OCP-E_{corr}*

Analysis of Variance

Source	Sum Sq.	d.f.	Mean Sq.	F	Prob>F
Grade	0.00025	2	0.00013	0.01	0.989
Temp	0.01229	1	0.01229	1.07	0.3065
Cl-	0.01123	1	0.01123	0.98	0.328
AcOH	0.01798	1	0.01798	1.56	0.2173
Grade*Cl-	0.02724	2	0.01362	1.18	0.3149
Grade*Temp	0.00481	2	0.0024	0.21	0.8121
Cl-*AcOH	0.05243	1	0.05243	4.56	0.038
Error	0.54036	47	0.0115		
Total	0.67563	57			

Constrained (Type III) sums of squares.

Figure 31: *ANOVA 2 model results for interactions between factors: Grade×Cl^-, Grade×Temp and Cl^-×AcOH. p-values indicates that Cl^-×AcOH was the only significant interaction (p=0.038).*

Analysis of Variance

Source	Sum Sq.	d.f.	Mean Sq.	F	Prob>F
Grade	0.00304	2	0.00152	0.13	0.875
Temp	0.00975	1	0.00975	0.86	0.3592
Cl-	0.0109	1	0.0109	0.96	0.3325
AcOH	0.01417	1	0.01417	1.25	0.2699
Grade*Cl-	0.02891	2	0.01446	1.27	0.29
Grade*Temp	0.00727	2	0.00363	0.32	0.7278
Cl-*AcOH	0.05134	1	0.05134	4.52	0.039
Grade*AcOH	0.02922	2	0.01461	1.29	0.2862
Error	0.51113	45	0.01136		
Total	0.67563	57			

Constrained (Type III) sums of squares.

Figure 32: *ANOVA 3 additional model, where Grade×AcOH interaction was not significant (p=0.286).*

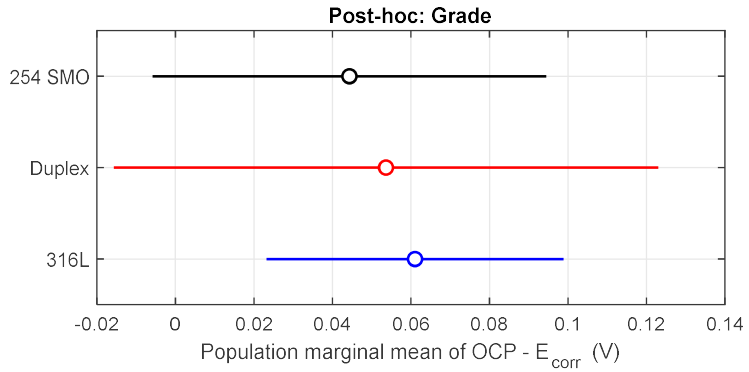

Figure 33: *Post-hoc between different SS grades. Mean values are close and intervals overlap between grades confirming no significant difference between grades in OCP-E_{corr}.*

A.4 Statistical Data for E_{pit} /E_{break}

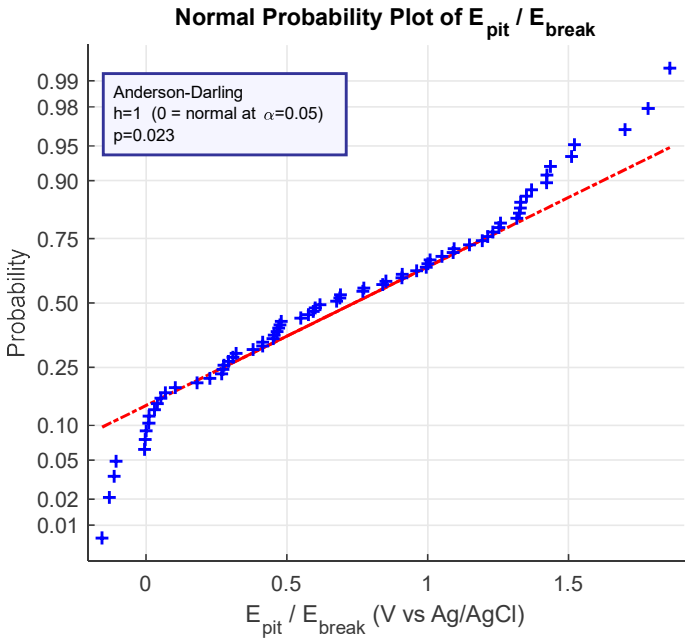

Figure 34: *Anderson-Darling test rejected normality at α=0.05. p-value for E_{pit} /E_{break} was 0.023 and h=1, which indicates that data does not follow a normal distribution. This is expected since corrosion resistance differs significantly between the tested SS grades.*

Analysis of Variance

Source	Sum Sq.	d.f.	Mean Sq.	F	Prob>F
Grade	10.6086	2	5.3043	146.02	0
Temp	5.8881	1	5.88811	162.09	0
Cl-	1.8759	1	1.87589	51.64	0
AcOH	0.0059	1	0.00587	0.16	0.6889
Error	2.3975	66	0.03633		
Total	20.7759	71			

Constrained (Type III) sums of squares.

Figure 35: *ANOVA 4 model results for single factors: Grade, Temp, Cl^- and AcOH. p-values are clearly below 0.05, indicating all single factors are significant regarding E_{pit} /E_{break}, except AcOH as a main effect.*

Analysis of Variance

Source	Sum Sq.	d.f.	Mean Sq.	F	Prob>F
Grade	10.6086	2	5.3043	257.29	0
Temp	5.8881	1	5.88811	285.61	0
Cl-	1.8759	1	1.87589	90.99	0
AcOH	0.0059	1	0.00587	0.28	0.5955
Grade*Cl-	0.4222	2	0.21112	10.24	0.0002
Grade*Temp	0.1859	2	0.09294	4.51	0.0151
Cl-*AcOH	0.0373	1	0.03731	1.81	0.1838
Grade*AcOH	0.5557	2	0.27787	13.48	0
Temp*Cl-	0.0006	1	0.00055	0.03	0.8706
Error	1.1957	58	0.02062		
Total	20.7759	71			

Constrained (Type III) sums of squares.

Figure 36: *ANOVA 5 model results for interactions between factors: Grade×Cl^-, Grade×Temp, Grade×AcOH, Cl^-×temp and Cl^-×AcOH. p-values indicates that Grade×Cl^-, Grade×Temp and Grade×AcOH were significant.*

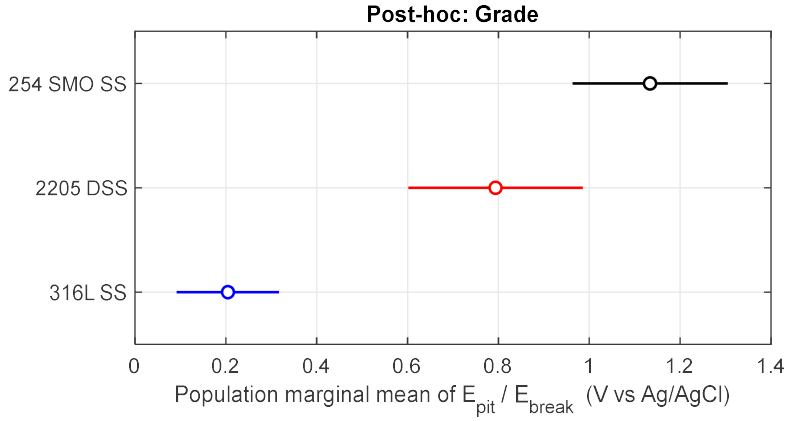

Figure 37: *Post-hoc of E_{pit} /E_{break} between SS grades. Mean values are clearly separated, and confidence intervals do not overlap. Values differ significantly from 316L SS to 2205 DSS and 254 SMO SS, indicating the hierarchy.*